GROWTH AND CHARACTERIZATION OF β-IRON DISILICIDE, β-IRON SILICON GERMANIDE, AND OSMIUM SILICIDES

Ryan James Cottier, B.S., M.S.

Dissertation Prepared for the Degree of

DOCTOR OF PHILOSOPHY

UNIVERSITY OF NORTH TEXAS

August 2009

APPROVED:

Christopher L. Littler, Major Professor and
Chair of the Department of Physics
Jose Perez, Committee Member
Arup Neogi, Committee Member
Michael Monticino, Dean of the Robert B.
Toulouse School of Graduate Studies

Cottier, Ryan James. Growth and Characterization of β-Iron Disilicide, β-Iron Silicon Germanide, and Osmium Silicides. Doctor of Philosophy (Physics), August 2009, 90 pp., 4 tables, 39 illustrations, references, 134 titles.

The semiconducting silicides offer significant potential for use in optoelectronic devices. Full implementation of the materials, however, requires the ability to tailor the energy gap and band structure to permit the synthesis of heterojunctions. One promising approach is to alloy the silicides with Ge. As part of an investigation into the synthesis of semiconducting silicide heterostructures, a series of β-Fe(Si1−xGex)2 epilayer samples, with nominal alloy content in the range $0 < x < 0.15$, have been prepared by molecular beam epitaxy on Si(100). I present results of the epitaxial and crystalline quality of the films, as determined by reflection high-energy electron diffraction, Rutherford backscattering spectroscopy, and double crystal x-ray diffraction, and of the band gap dependence on the alloy composition, as determined by Fourier transform infrared spectroscopy. A reduction in band gap was observed with increasing Ge content, in agreement with previous theoretical predictions. However Ge segregation was also observed in β-Fe(Si1−xGex)2 epilayers when $x > 0.04$.

Osmium silicide films have been grown by molecular beam epitaxy on Si(100). The silicides have been grown using e-beam evaporation sources for both Os and Si onto Si(100) substrates at varying growth rates and temperatures ranging from 600-700ºC. The resulting films have been analyzed using reflection high-energy electron diffraction, Raman spectroscopy, reflectivity measurements, in-plane and out of plane X-ray diffraction and temperature dependent magnetotransport.

A change in crystalline quality is observed with an increase in Si overpressure. For a lower silicon to osmium flux ration (JSi/JOs=1.5) both OsSi2 and Os2Si3 occur, whereas with a much larger Si overpressure (JSi/JOs>4), crystalline quality is greatly increased and only a single phase, Os2Si3, is present. The out-of-plane X-ray diffraction data show that the film grows along its [4 0 2] direction, with a good crystal quality as evidenced by the small FWHM in the rocking curve. The in-plane X-ray diffraction data show growth twins with perpendicular orientation to each other.

TABLE OF CONTENTS

LIST OF TABLES

LIST OF FIGURES

CHAPTER 1

INTRODUCTION

Background

Silicon is still the material of choice for most microelectronic applications due to the low cost of material and advanced manufacturing technology and processes that are available. Unfortunately, due to its indirect bandgap, it is not the ideal choice for many optoelectronic applications. To bridge this gap, what is needed is a direct bandgap material that can be directly integrated into silicon technology for optoelectronic applications. This would aid in a number of critical applications such as near infrared thermal sensing, optical interconnects for silicon based chips, and fiber optical communication in the low loss 1.3 to 1.6 micron region. Much research has gone into developing methods of creating optically active silicon devices to fulfill the optoelectronic needs.

Some of the more successful methods include band structure engineering via alloying, atomic layer superlattices, luminescence via impurity centers, silicon nanoparticles, polymers and molecules containing silicon, hybrid methods for integrating direct gap materials with Si, and dislocation engineering.[1] Most of these methods have significant limitations and remain in the developmental stages. The following is a brief review of these methods along with achievements and limitations in these areas.

Alloying of Silicon

Ge and C alloyed with Si allow engineering of the electronic band structure by varying the energy gap through adjustment of alloy composition. $Si_{1-x}Ge_x$ alloys grown on Si substrates have a tenability range relevant to fiber optic communications needs. However, severe limitations are involved including a limited critical thickness which results in size limitations of infrared detectors and emitters, and the bandgap remains indirect.[1] Ultimately, present devices developed from Si alloys are still not practical due to their low luminescent efficiency at room temperature.[2,3]

Introduction of Impurities

Another approach to increasing the electroluminescence efficiency of indirect bandgap semiconductors is to introduce impurity levels into the bandstructure as has been researched in Si by doping with rare earth impurities (erbium for instance),[4] carbon complexes,[5] and sulfur-oxygen complexes[6] as localization centers for electron-hole recombination. Optical emission from Si doped with the Er^{3+} ion occurs near 1.5 μm, again in the range relevant for fiber optic technology.[1] This approach is limited by the low quantum efficiency for higher temperatures and a marked quenching of the luminescence for temperatures above ~150 K.[7,8]

Nanostructures of Si

Nanostructures of Si have been considered due to the effects of confinement on carrier wavefunctions when the crystallite diameter is less than the size of the free exciton Bohr radius of 4.3 nm in bulk c-Si.[9] Quantum confinement increases the

electron-hole wave-function overlap, resulting in increased light emission efficiency and shifts the emission peak to higher energy.[10,1] Nanostructures of Si have been created using porous Si, Si nanoclusters, and Si quantum wells, wires and dots.

Si-Ge thin layer superlattices were theorized to possibly result in a quasi-direct band gap due to Brillouin zone folding.[11] High quality Si/Ge superlattice layers on the order of several monolayers were grown by molecular beam epitaxy.[12] Infrared emission at fiber optic transmission relevant energies can be obtained from these superlattices, but only at low temperature. These atomic layer superlattices will most likely find eventual use as infrared detectors rather than emitters unless there are further major improvements in material quality.[13,14,1]

Porous Si, pi-Si is created using electrochemical dissolution in HF based electrolytes.[1] This leaves an array of deep, narrow pores generally perpendicular to the surface of the Si. This process can be used to produce an irregular array of undulating freestanding pillars of c-Si only nanometers wide.[15] Canham [15] observed intense visible PL at room temperature from pi-Si that had been etched under carefully controlled conditions. Visible luminescence ranging from green to red in color was reported by Cullis [16] for other pi-Si samples and attributed to quantum size effects in wires of width ~3 nm.[15] Another group reported a Si absorption edge at values as high as 1.76 eV that they attributed to quantum wire formation.[17] Visible PL in pi-Si at room temperature was reported by Bsiesy [18] and Koshida [19]. A strong PL signal has been observed from pi-Si at wavelengths from near infrared through visible to blue allowing for the creation of white light emitting pi-Si.[1]

Thin QWs of Si separated by wide band gap barriers have been investigated, and visible light emission at room temperature has been shown in Si/SiO_2 superlattices grown by molecular beam epitaxy,[20] and the indications of direct band-to-band recombination were confirmed by measurements via X-ray techniques of the conduction and valence band shifts with layer thickness.[20] Several groups have investigated quantum wires obtained by etching $Si/Si_{1-x}Ge_x$ heterostructures.[21,22] In PL measurements, wires defined by electron beam lithography and reactive ion etching have shown small blue shifts of up to 30 meV in the $Si_{1-x}Ge_x$ alloy peak at ~1.1 eV due to a combination of strain and confinement.[1] Also, $Si_{1-x}Ge_x$ wires have been grown on V-groove patterned Si substrates.[23] No significant intensity enhancements compared with PL from QW transitions have been realized in these wire structures.[1] More attention has been turned to the production of $Si_{1-x}Ge_x$ quantum dots, as these produce the strongest confinement effects for a given diameter or can achieve desired confinements with smaller diameters than for wires[1] Quantum dots fabricated by etching $Si/Si_{1-x}Ge_x$ superlattices have produced 4 K PL at 0.97 eV that is 200 times brighter in 60 nm dots compared with the unetched superlattice PL.[24] Similar studies of $Si_{1-x}Ge_x$ dots fabricated by self-assembling island growth on Si has shown an increased luminescence efficiency due to the localization of excitons in the dots.[25] In both cases, EL has been observed from diode structures at low temperatures[24, 25] and at room temperature.[24] It is conceivable that this work could lead to a new generation of $Si/Si_{1-x}Ge_x$ optoelectronic devices at the optical fiber communication wavelength of 1.3 um.[1]

Silicon Based Polymers

Bright visible luminescence has been found in a number of Si polymer and molecular compounds.[26] The most prominent of these is siloxene, $Si_6O_3H_6$[27] and polysilane and its polymer derivatives.[1] Siloxene has a direct bandgap [28] and the PL can be wavelength tuned across the visible region, [29] but its chemical instability at higher temperatures limits its practical usefulness in devices requiring thermal processing.[1] One form of polysilane exhibits a direct bandgap of 3.9 eV and efficiently emits ultraviolet light.[26] However, Si polymers require much more developmental work before they can be considered for ultraviolet devices based on Si.[1]

Dislocation Loops in Silicon

Efficient silicon-based light emitting diodes fabricated using dislocation engineering have recently been reported.[30] Boron was implanted into n-type silicon (100) substrates followed by high temperature annealing. The boron introduces dislocation loops as well as p-type dopant to form a p-n junction. PL and EL emissions were obtained with a dominant peak at ~1154 nm.

Hybrid Methods

Silicon based lasers and other light emitters remain unavailable for on-chip optoelectronic applications. This has led to significant work in combining III-V semiconductor laser diodes with Si integrated circuits for optical fiber communications or optical interconnects. This requires the growth of III-V materials such as GaAs or

InP on Si followed by processing, or the direct bonding of preconstructed III-V laser devices.[31,32] The lattice mismatch of the two materials with Si creates high defect densities, making laser applications difficult. Further the difference in thermal expansion coefficient creates problems at the increased operating temperatures. This work has led to 1.5 um wavelength InGaAs/InGaAsP multiple QW laser operating continuously at room temperature on a Si substrate.[33]

Semiconducting Silicides

One avenue which has been sparsely studied is the twelve semiconducting silicides which provide a promising material set for optoelectronic devices that can be directly integrated with silicon manufacturing technology. Fundamental energy gaps of the known semiconducting silicides range from 0.07-0.12 eV (hexagonal $MoSi_2$ and WSi_2, $ReSi_2$) to 2.3 eV ($OsSi_3$). They may provide a background for energy-gap engineering comparable to that achieved with $A^{III}B^{V}$ compounds in their superlattices.[34] Ternary silicides are attractive for possible regulation of the fundamental electronic properties and for epitaxial matching of semiconducting silicide films. An appropriate systematic study of these materials has not been accomplished,[34] but of these materials, the semiconducting phase of iron disilicide, β-$FeSi_2$, has been the most studied. Recent data has shown about 50 times higher optical absorption coefficient as compared to crystalline silicon.[35] In addition, both electroluminescent[36] and photovoltaic[35] devices have been demonstrated in this material.

Previous optical measurements of β-$FeSi_2$ have shown both indirect and direct transition behavior depending on the preparation method.[34] Theoretical calculations show an indirect transition at 0.76 eV and a direct transition 0.87eV.[37] However, strain in the lattice can lower the direct band energy below the indirect transition resulting direct band gap behavior and light emission at 1.5 um.[38] β-$FeSi_2$ is closely lattice matched with Si (001) with a mismatch of 2% or -4%, depending on the azimuthal orientation.[39] This is consistent with reports of samples containing small precipitates of β-$FeSi_2$ embedded in single crystalline silicon having intense luminescence indicating a direct band gap while other more uniform growths of β-$FeSi_2$ do not.[40] To date, luminescence from this material has been rather poor and needs to be improved for room temperature operation. For continued improvement in the performance of β-$FeSi_2$ as a near IR detector and emitter, improved deposition processes are needed to ensure consistent strain and thus consistent direct band gap performance. A more in-depth discussion of β-$FeSi_2$ can be found in Chapter 3.

Little data is available on the other semiconducting silicides. These silicides have relatively high thermal stability, the ability to withstand normal Si fabrication processes, and the ability to form a passivating SiO_2 layer, through standard oxidation. Table 1.1 (adapted from [34]) organizes some of the principal parameters (crystal group, lattice parameter, theoretical and experimental bandgap and associated references) for the semiconducting silicides. Listed in Table 1.2 are several silicides paired with germanide analogues. Functional heterostructures for electrical and electro-optical applications (i.e. QW's and lasers) require similar crystal structures and lattice parameters. Further,

the probability of success in alloying and lack of miscibility gaps is greatly improved. Therefore groups A, B, and C of Table 1.1 group like materials for closer comparison.

As seen in group A, $OsSi_2$ may be a good candidate for alloying with β-$FeSi_2$ as well as for the creation of β-$FeSi_2$ and $OsSi_2$ heterostructures since $OsSi_2$ is isostructural to β-$FeSi_2$ with a maximum mismatch of 5%. Theoretical studies using full-potential linearized augmented plane wave method have shown that the ternary $Os_{0.5}Fe_{0.5}Si_2$ may have a direct gap of 0.78 eV.[41] β-$FeSi_2$ is known to be direct band gap (quasidirect), at around 0.8-0.87 eV,[34] and the experimental data suggests that $OsSi_2$ may have a direct band gap out to 1.8 eV.[57] If the proper valence offsets exist, this pair may allow for a reasonable heterostructure device. Theoretical calculations of the $OsSi_2$ band structure show a band gap of 0.06 eV, contrasting greatly with the experimentally observed 1.4-1.8 eV value.[42] Little experimental work has been performed on this potentially valuable material.

Group B includes $MoSi_2$, WSi_2, and $CrSi_2$, which also appear to be candidates for heterostructure combination. These have band gaps reported to range from 0.07eV ($MoSi_2$, WSi_2) to 0.5 or 0.98 eV for $CrSi_2$. Both theory and experiment indicate that $CrSi_2$ may have a direct band gap. The maximum lattice mismatch between the three is 2.5%. Thus this system may allow for engineering of binary-binary heterostructures with large offsets, but also potentially allow for tunable emitters from ~1 eV down to narrow band gap through variation of the $CrWSi_2$ alloy.

Group C compares Ru_2Si_3 and Os_2Si_3 which may have the potential for an alloy system. Os_2Si_3 has had a experimentally reported band gap of 0.95 and 2.3 eV

depending on the source. Ru_2Si_3 has experimental values ranging from 0.44 to 1.1 eV, and theory predicting a direct gap at 0.4eV. Both materials have the *Pbcn* space group, and are lattice matched very well (0.6%).

Objectives

The objective of this study is to explore further the feasibility of select semiconducting silicides for use in optoelectronic applications. In particular, β-$FeSi_2$, β-$Fe(SiGe)_2$, multiphase $OsSi_2$ and Os_2Si_3, and single phase Os_2Si_3 thin films have been prepared using molecular beam epitaxy and characterized using a variety of experimentation methods. Chapter 2 will discuss the methodology and equipment, including molecular beam epitaxy, electrical characterization by Hall effect measurements, optical characterization by Fourier transform infrared absorption spectroscopy and structural characterization by x-ray diffraction. Chapter 3 will discuss the previous studies of β-$FeSi_2$ and the MBE growth and characterization of β-$FeSi_2$ and β-$Fe(SiGe)_2$ over a range of Ge concentration (0-5%). Chapter 4 will cover the previous work on the osmium silicides and discuss the MBE growth of Os_2Si_3 films and multiphase osmium silicide films and their characterization. An overview and conclusions are given in Chapter 5.

Table 1.1 Summary of the semiconducting silicides with emphasis on similarities of crystalline properties, adapted from Borisenko[34].

Group	Phase	Structure	Space Group	Lattice	Lattice Parameters (nm)			Exp. E_g	Type of Gap (Expl)	Theoretical E_g	Type of Gap (Theoretical)
					a	b	c				
A	β-$FeSi_2$	β-$FeSi_2$	Cmca	Orthorhombic	0.98792 [43]	0.77991	0.78388	0.87[44]	Direct	0.78[45]	Quasi-direct
	$OsSi_2$	β-$FeSi_2$	Cmca	Orthorhombic	1.0150 [46]	0.8117	0.8223	1.4[47]		0.95[48]	Indirect
								1.8[49]		1.14[48]	Direct
B	$CrSi_2$	$CrSi_2$	$P6_222$	Hexagonal	0.4431 [43]		0.6364	0.35 [50]	Indirect	0.21 to 0.38[51,49,52]	Indirect
								0.5[50]	Direct	0.37 to 0.47[51,49,52]	Direct
								0.67[53]	Indirect		
								0.98[53]	Direct		
	$MoSi_2$	$CrSi_2$	$P6_222$	Hexagonal	0.4642 [43]		0.6529	0.07[54]	Indirect		
	Wsi_2	$CrSi_2$	$P6_222$	Hexagonal	0.4614[46]		0.6414	0.07[54]	Indirect		
C	Ru_2Si_3	Ru_2Si_3	Pbcn	Orthorhombic	1.1057[55]	0.8934	0.5533	0.44[51]		0.40	Direct
								0.7[51]			
								1.09[56]			
	Os_2Si_3	Ru_2Si_3	Pbcn	Orthorhombic	1.1124[46]	0.8932	0.5570	2.3[49]			
								0.95[57]	Direct		
D	OsSi	FeSi	$P2_13$	Cubic	0.4729[46]			0.34[49]			
	Os_2Si_3	Ru_2Si_3	Pcbn	Orthorhombic	1.1124[46]	0.8932	0.5570	2.3[49]			
								0.95[57]	Direct		
	$OsSi_2$	β -$FeSi_2$	Cmca	Orthorhombic	1.0150[46]	0.8117	0.8223	1.4[47]		0.95 [48]	Indirect
								1.8[58]		1.14[48]	Direct
E	Ir_3Si_5		$P2_1/C$	Monoclinic	0.6406[59]	1.4162	1.1553	1.2[60]	Direct		
								1.37[61]	Direct		
	Mg_2Si	CaF_2	Fm3m	Cubic	0.63512[43]			0.78[62, 63]	Indirect		
	$BaSi_2$	$BaSi_2$	Pnma	Orthorhombic	0.892[64]	0.680	1.158	0.48[43]			
								1.3[47]			

Table 1.2. Silicides paired with germanide analogues. Many of the germanides are of similar crystal structure to the silicides.

Phase	Structure	Space Group	Lattice	Lattice Parameters (nm)		
				a	b	c
β-$FeSi_2$	β-$FeSi_2$	Cmca	Orthorhombic	0.98792[43]	0.77991	0.78388
$FeGe_2$	$FeSi_2$	C16	Tetragonal	0.5908[65]		0.4955
$BaSi_2$	$BaSi_2$	Pnma	Orthorhombic	0.892[64]	0.680	1.158
$BaGe_2$	$BaSi_2$	Pnma	Orthorhombic	0.905	0.683	1.124
Ru_2Si_3	Ru_2Si_3	Pcbn	Orthorhombic	1.1057[55]	0.8934	0.5533
Ru_2Ge_3		Pcbn	Orthorhombic	1.1436	0.9238	0.5716
Os_2Si_3	Ru_2Si_3	Pcbn	Orthorhombic	1.1124[46]	0.8932	0.5570
Os_2Ge_3	Ru_2Si_3	Pcbn	Orthorhombic	1.1544	0.9281	0.5783
$OsSi_2$	ß-$FeSi_2$	Cmca	Orthorhombic	1.0150[46]	0.8117	0.8223
$OsGe_2$	$OsGe_2$	C2/m	Monoclinic ß=119°10′	0.8995	0.3094	0.7685

CHAPTER 2

THEORETICAL CONSIDERATIONS, METHODOLOGY, AND EQUIPMENT

Semiconductor Band Structure

The energy $\varepsilon(k)$ of the electron states within a solid as a function of the wave vector k is called the band structure and is necessary for determining the electronic properties of the material. The origin and significance of band structure can be understood, following the reasoning of Omar [66], by first considering the energy spectrum for a single atom, then a molecule, and finally a solid.

The wave function of the electrons in an isolated atom can be determined by solving the Schroedinger equation:

$$H\Psi = E\Psi$$

where H is the Hamiltonian operator. A fundamental outcome of quantum mechanics is that the wave solutions of this equation produces eigenvalues, E_n, which correspond to values of a discrete energy spectrum unlike the continuous energy spectrum which almost always results from classically computed mechanics. Due to the discrete nature of the solutions, the electrons themselves can only exist with specific values of energies, meaning their possible energies are quantized. For instance, the lithium atom, separated from any outside influence, will have its first three states, in order of increasing energy, labeled 1s, 2s, and 2p, where the numbers specify the particular quantum state and the letters specify the specific angular momentum state. The illustration of these states in Figure 2.1a shows the ladder type arrangement resulting

from this outcome.[66]

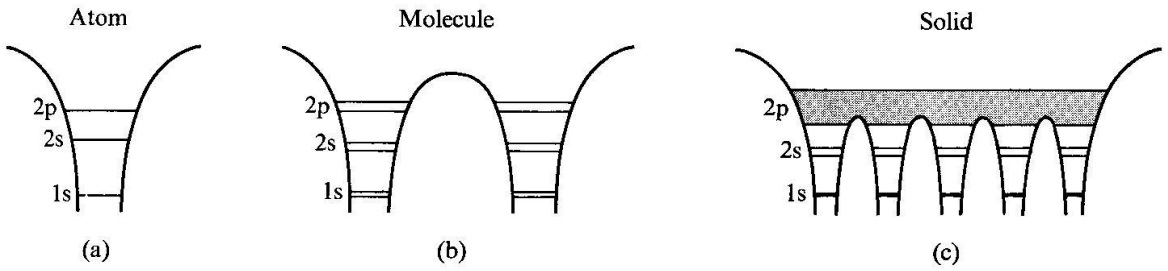

Figure 2.1. The evolution of the energy spectrum of Li from an atom (a), to a molecule (b), to a solid (c) [66].

According to quantum mechanics and the Pauli exclusion principle, no two electrons can be in the same state. Quantum states can be further specified by another property, labeled spin, of which there are only two choices, spin up and spin down. Therefore, at most, two electrons can be in the 1s state as long as their spins are opposite. The same is true for 2s, 2p, and all other possible states. The lithium atom has three electrons, which are, at low temperatures, distributed as the following: two in the 1s state and one in the 2s state.[66]

In creating the Li_2 molecule, the lithium atoms, initially at a distance allowing no interaction, are slowly brought together. As the individual atoms begin to interact, the energy states split into doublets of similar but slightly different energy, as shown in Figure 2.1b. The states split further as bonding with other Li atoms occurs. As the number of atoms increases to $\sim 10^{23}$, roughly the number of atoms in a macroscopic solid, shown in Figure 2.1c, the quantum states split so many times that the difference in energy between consecutive split levels is small enough to consider the energy

continuous within that level.[66] These energy states then make up a series of energy bands which are each separated by a gap. Using similar quantum mechanical calculations, one can determine a bulk material's band structure, (i.e. the energy, $\varepsilon(k)$, of the electron states as a function of the wave vector, k). The splitting of energy levels and the formation of bands for the diamond structure is depicted in Figure 2.2.[67]

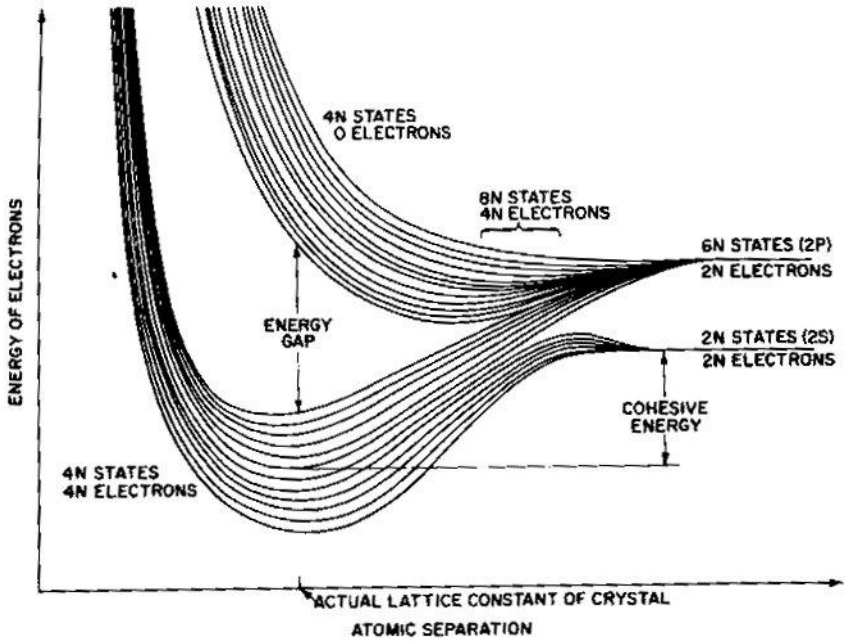

Figure 2.2 Electron energy levels as a function of lattice constant for diamond demonstrating banding [67]

The electrical nature of a material is directly associated with the calculated band structure. Conducting materials allow electrical current to flow freely when an electric field is applied. An insulator, however, strongly resists any electric current. It follows from band structure calculations that this results from how full particular bands. The requirement for electron flow is simply that an empty state exists and is accessible by a

previously bound electron so that the electron may enter that new state. In a metal, one band of electronic states is only partially full of electrons; therefore, it takes only an infinitesimal increase in energy for the most energetic electrons to enter new states, and therefore move freely throughout the solid.[66] In an insulator, one band, called the valence band, is completely filled with electrons, while the band above it in energy, the conduction band, is completely empty.[66] The difference in energy between the top of the valence band and the bottom of the conduction band, the fundamental energy gap (or band gap), is too large for electrons to jump across easily. A semiconductor is similar to an insulator in that its valence band is completely full and the conduction band is completely empty.[66] However, the band gap is of the order of 1 electron volt, small enough to allow some electrons to be thermally excited to the conduction band. Since both the valence and conduction bands then are only partially full, they become conducting.

For semiconductors, the dispersion law can be calculated be assuming a parabolic band for the conduction and valence bands. If the top of the valence band and the bottom of the conduction band are at the same point in k-space, the energy gap is labeled direct, shown in Figure 2.3a, and if they are at different points the gap is labeled indirect (Figure 2.3b).[67]

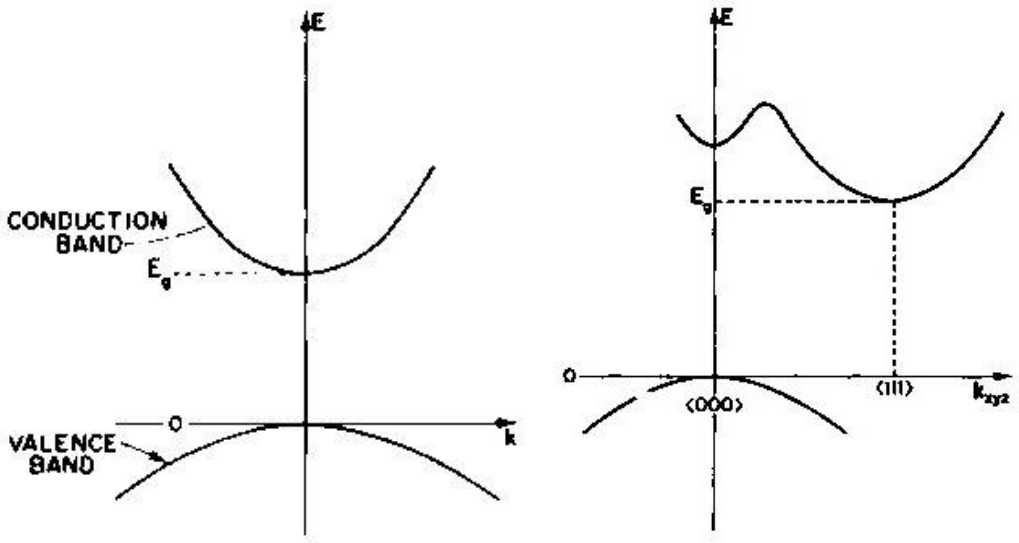

Figure 2.3. Energy vs. momentum in (a) a direct gap semiconductor and (b) an indirect gap semiconductor with a conduction band valley at k = <000>[67].

Molecular Beam Epitaxy

Molecular beam epitaxy (MBE) was first discussed in 1970 after the technique was developed through the late 1960's by Alfred Y. Cho of Bell Laboratories as a growth method for high quality epitaxial layers.[68] MBE allows for precise control of single crystal layer growth within a non-equilibrium environment. First used as a method of growing GaAs layers, MBE has developed as an optimal technique for the growth of semiconducting, metallic, and insulating materials as well as high-quality multilayer devices, and is a preferred method for many applications in both academia and industry.

MBE is an evaporation process whereby elements or compounds are vaporized into atomic or molecular beams directed at a temperature controlled crystalline

substrate in an ultra-high vacuum environment. The incident atoms/molecules then continue the crystal structure of the substrate creating an epitaxial layer. If the new crystalline layer is of the same chemical composition as the substrate, homoepitaxy occurs, whereas growth of a layer with differing composition is heteroepitaxy.

MBE differs from other vacuum deposition techniques due to the extreme precision allowed through controlling beam flux and other growth conditions. Further, the nature of MBE growth results in non-equilibrium conditions whereas liquid phase epitaxy and vapor phase epitaxy proceed at (and are limited by) thermodynamic equilibrium.[69]

Epitaxial Growth Modes

The growth of epitaxial layers follows one of several growth modes, illustrated in Figure 2.4.[67] Volmer-Weber mode refers to island like growth where the bonding of the film is stronger than the bonding to the surface of the substrate. The Frank-van der Merwe growth mode is often referred to as layer-by-layer growth since the epitaxial film preferentially bonds to the substrate. This results in single layers being filled before a new layer is started.[67] Molecules which do begin new layers before the previous layer is complete are able to move around enough, due to thermal energy, to reposition into the unfilled layer. Stranski-Krastanov describes a growth process which is a mixture of the Volmer-Weber and Frank-van der Merwe modes where initially, layer-by-layer growth is preferential, but the film strain is high and results in island growth after some layer thickness is achieved.[67] Step Flow growth mode is seen in offcut

substrates where the growth at atomic layer steps is preferred. Therefore layers grow outward from the atomic layer steps. Columner growth begins like the island growth method but the islands never coalesce.[67] The resulting growth mode of a material system can vary greatly by adjustment of any of the growth conditions like substrate temperature, partial pressure of incident beams, or substrate preparation.

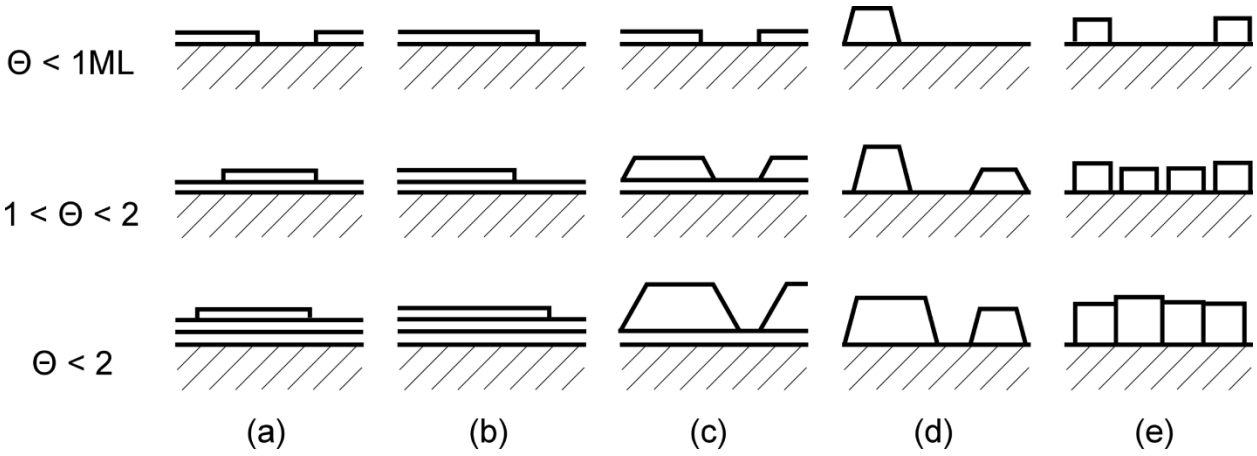

Figure 2.4 Growth modes: (a) Frank-van der Merwe, (b) step flow (c) Stranski-Krastanov (d) Volmer-Weber and (e) columner.[69]

Lattice Mismatch and Strained Layers

Heteroepitaxial growth depends strongly on whether the grown epilayer is coherent or incoherent with the substrate. Coherence occurs when the crystallographic structure is perfectly continued at the interface.[70,71] If the overgrowth is incoherent with the substrate, then it is free to adopt any in-plane lattice constant that minimizes its free energy. If the overgrowth is coherent with the substrate, then energy minimization is achieved by adopting the in-plane lattice constant of the substrate, thus creating a commensurable material system with the substrate. The resulting elastic strain energy can then increase its overall free energy significantly.[72] Both of these

growth processes are often applied for preparation of semiconductor devices, when using different epitaxial growth techniques.

Heteroepitaxial growth is strongly dependent on lattice mismatch as shown in Figure 2.5.[73] Experimental data indicates that epitaxy can result if the lattice misfit, defined as $100(a_f-a_s)$, where a_s and a_f are the lattice constants in the substrate and the film, respectively, is not larger than 15%.[74,75] If the misfit between a substrate and an epilayer is sufficiently small, the first atomic monolayers which are deposited will be strained to match the substrate and a coherent epilayer will be formed.[76,77] As layer thickness increases, the homogeneous strain energy becomes so large that a thickness is reached when it is energetically favorable for misfit locations to be introduced. The overall strain will be reduced, but the dislocation energy will increase. This critical thickness was shown theoretically by van der Merwe[78] and confirmed experimentally.[79]

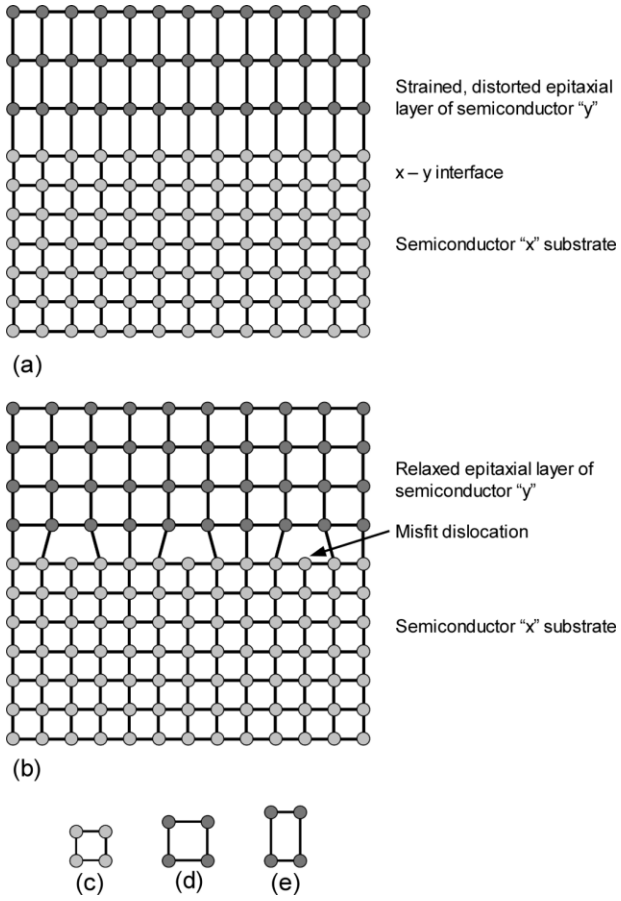

Figure 2.5. Heteroepitaxial growths resulting in (a) compressive strain and (b) misfit dislocations due to relaxation. (c) represents the size of the substrate unit cell, (d) represents the size of the unstrained film's unit cell, and (e) represents the strained film unit cell.[69]

The possibility of growing high-quality epitaxial layers of different materials on lattice mismatched substrates is a topic of considerable interest for the growth of heterostructures.[The range of useful devices available with a given substrate is largely enhanced by this method. For example, GaAs and compounds related to it (AlGaAs, InGaAs, etc.) offer many advantages over Si in terms of increased speed and radiation resistance and its ability to process and transmit signals by light pulses.[73] Si, on the other hand, is a well-established material for integrated circuits and exhibits superior mechanical and thermal characteristics. By growing, for example, epitaxial

layers of GaAs on Si substrates, it would be possible to combine the advantages of both materials.[73] However, these materials are not matched together, neither by lattice constants (a_{Si} = 0.543 nm, a_{GaAs} = 0.565 nm), nor by thermal expansion coefficients (α_{Si} = 2.6x10^{-6} K^{-1}, α_{GaAs} = 6.8x10^{-6} K^{-1}).[73] Therefore dislocations and other lattice defects are usually present in GaAs/Si heterostructures.[

Strain also plays a dominant role in determining the alignment of energy bands at hetero-interfaces, thus determining the confinement energy of electrons or holes in quantum wells.[80] For instance multilayered strained structures of Si and $Si_{1-x}Ge_x$ alloys are used to create electron/hole quantum wells.[Heteroepitaxy and heterostructures have become the basis of present day semiconductor optoelectronics and have opened the way to development of nanoscale electronics.[73][

MBE Equipment and Techniques

MBE is performed under ultrahigh vacuum, and has the advantage of being controlled by in situ techniques such as reflection high energy electron diffraction (RHEED), reflection mass spectrometry, reflectance anisotropy spectroscopy, spectroscopic ellipsometry, and laser interferometry.[73]

A schematic of the MBE system used in this study is shown in Figure 2.6. This chamber was donated to the University of North Texas by Hans Gossmann of Bell Labs in 2002.

Effusion cells are mounted radially around a variable temperature substrate mount. Since growth is usually of the order of Å/s, the background pressure in the

chamber must be maintained at ~10^{-11} Torr in order to reduce film impurities. In situ monitoring of the crystalline nature of the film can be accomplished through the use of RHEED whereby an electron beam at a low angle to the substrate diffracts with the surface atoms. The diffraction pattern produced has direct information about the surface reconstruction as well as the shape of the surface.

The MBE system was maintained at ultra-high vacuum first by rough pumping using a dry scroll pump to ~10 mTorr. Three cryogenic pumps and an ion pump were then engaged while a removable box enclosing the system was heated to ~180ºC to remove gases absorbed in the surfaces. This temperature was maintained for at least 24 hours. The heaters were then turned off and the box removed, allowing the pumps to reduce the pressure to ~10^{-10} Torr, measured by ion gauge. Liquid nitrogen was then circulated through a cryo-shroud, dropping the chamber pressure to ~10^{-11} Torr.

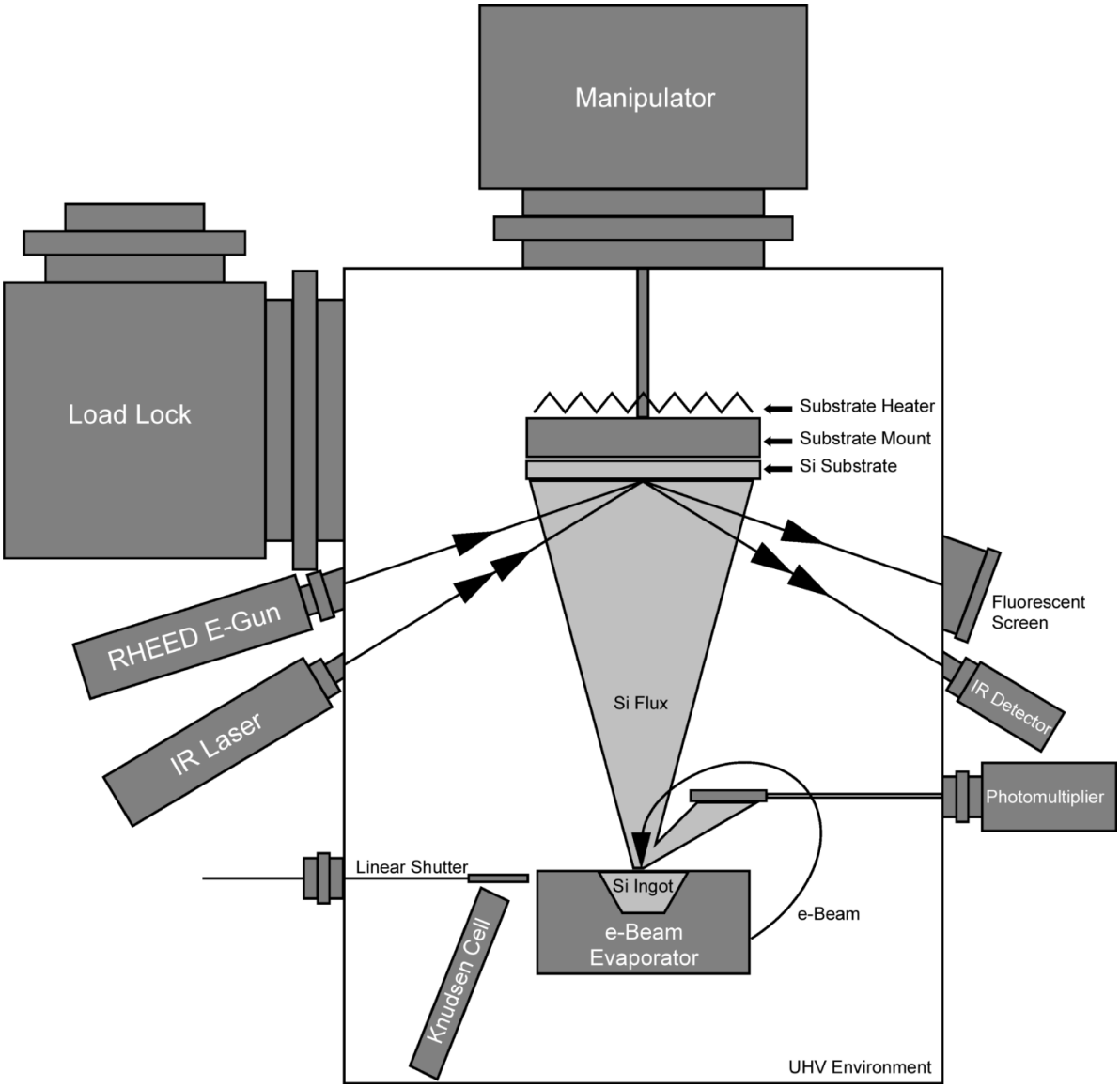

Figure 2.6. Schematic of the MBE system used in this study.

Two inch silicon (100) wafers, both n and p type were prepared using the method described by Shiraki.[133] This included a series of acid and base baths to develop a SiO_2 layer on the wafer surface. After each oxide growth, the oxide was etched off using hydrofluoric acid, and therefore surface impurities were removed. After several oxide layer growth and etching cycles, a final oxide layer was formed. At

this point, the wafer was mounted on a molybdenum sample holder and inserted into the load-lock section of the MBE system.

The sample and sample holder were then transferred into the main section where it was mounted on the sample manipulator. This manipulator had x, y, and z directional movement as well as rotation about axes both normal and parallel to the substrate surface. On the sample manipulator was a laser-cut graphite coil with electrical leads that acted as a heater. The Si substrates used were double-side-polished, which allowed for temperature calibration of the sample by using an IR laser. The laser was aimed at an angle towards the middle of the sample. Reflections off the front and back surfaces were collected using a diode. Given a particular temperature change and the thermal expansion coefficient of Si along the (100) direction, the change in thickness can be calculated. This change in thickness translates to a change in path length of the light reflected off the back surface, and therefore, interference fringes are detected and counted using computer software. For each sample, the computer steps through different heater current values, counts fringes, and determines a current-temperature calibration curve, allowing a temperature calibration within ±1°C.

Typically MBE systems have a molecular beam path length (form source to substrate) on the order of ~20 cm. In order to maintain uniformity of the grown layers, the substrates are continuously rotated around the normal during growth. The system used in this study had a path length of ~1 m. This large distance allowed for the substrate to remain stationary throughout growth.

Molecular sources used were e-beam evaporators and effusion cells. One e-beam evaporator was always used to provide 99.999% ("five nines," 5N) pure Si. Another e-beam evaporator provided Fe (3N8) or Os (3N) depending on the intended epitaxial film. Effusion cells were used for Ge (6N) and Fe (3N8) at times.

The e-beam evaporators operated by accelerating a beam of electrons toward the source material using high voltage. This beam was steered by two electromagnets which provided x and y steering. The steering magnets could be oscillated individually allowing for the evaporation area and shape to be adjusted.

The Si evaporation rate was calibrated using RHEED intensity oscillations. RHEED images were monitored using a CCD camera, and image processing software recorded the intensity of the characteristic epitaxial RHEED streaks in time. This data was analyzed using Fourier Transform to determine the growth rate in monolayers/sec. One monolayer corresponds to 1.3 Å/s for Si (100), hence the growth rate was established. Fe, Os, and Ge were determined using Rutherford Backscattering *ex situ*. Once calibrated, growth of epilayers was performed using computer controls of the e-beam power, effusion cell temperature, linear shutters over each source, and the substrate heaters. A Sun-2 computer with custom software operated through a VMEbus for this control.

Electrical Characterization

E.H. Hall discovered that a magnetic field applied perpendicular to the direction of current flow within a solid would result in an electric field perpendicular to both the

magnetic field and the current.[81] Measuring this Hall voltage has become a standard route of electrical characterization of semiconductors.

The Hall effect derives from the nature of the magnetic force on moving charges as described by the Lorentz equation, $\mathbf{F}_m = -q(\mathbf{v}\times\mathbf{B})$, where $\mathbf{v}$ is the velocity of the moving charge, q. The cross product implies the Lorentz force acts perpendicular to both the magnetic field $\mathbf{B}$ and $\mathbf{v}$. Due to the finite physical boundaries of a solid, charge carrier motion is restricted causing electrons to accumulate at one side of the material. However, in a solid, motion in this direction is restricted by the boundaries of the solid and thus the electrons accumulate at one side of the material. As a result of the separation of charge an electric field transverse to both $\mathbf{B}$ and $\mathbf{v}$ is set up which counterbalances the Lorentz force. The electron drift velocity is proportional to $\mathbf{E}$ and is described by

$$\mathbf{v}_d = \mu_d \mathbf{E}$$

where μ_d is the carrier drift mobility and $\mathbf{E}$ is the electric field. The value μ can also be defined and measured from the current density, $\mathbf{J}$:

$$\mathbf{J} = \mu_c n q \mathbf{E}$$

where n is the carrier concentration, μ_c is the conductivity mobility (which in principle should be equal to μ_d), and q is the electron charge. The resistivity ρ of a semiconductor can be written as

$$\rho = 1/\mu_c n q$$

The Hall coefficient, R_H, is defined as

$$E_H = R_H IB/A$$

where I is the current flow through the sample, A is the cross section, and d is the thickness and B is the magnetic field. The Hall coefficient is related to the carrier concentration by

$$R_H = -r_n/\mathrm{nq},\ r_p/pq$$

where q is the electron charge and n or p is the density of electron or holes, respectively and r_n or r_p is a constant that depends on the dominant scattering mechanisms and can be studied by the temperature dependence of the Hall mobility. For semiconductors, r_n or r_p is generally equal to unity. A measurement of resistivity and carrier concentration will give the Hall mobility of the majority carriers in the semiconductor, defined as

$$\mu = R_H \sigma$$

The Hall voltage, V_H, is defined as

$$V_H = R_H IB/d$$

where the amplitude and polarity depends on the magnitude and polarity of I and on the direction of B.

A schematic diagram of the sample geometry is shown in Fig 2.8.[82] If terminal 1 is the positive polarity for a DC current I + and the direction of the magnetic field as shown is defined as B +, then the Hall voltage measured between terminals 3 and 4 is such that terminal 3 is negative for an n-type material (electrons are the majority carrier) and positive for a p-type material (holes are the majority carrier. The Hall

contacts are point contacts placed on the surface so that $VH = 0$ when $B = 0$. In actulity, there will always be a misalignment potential. Therefore, the potential

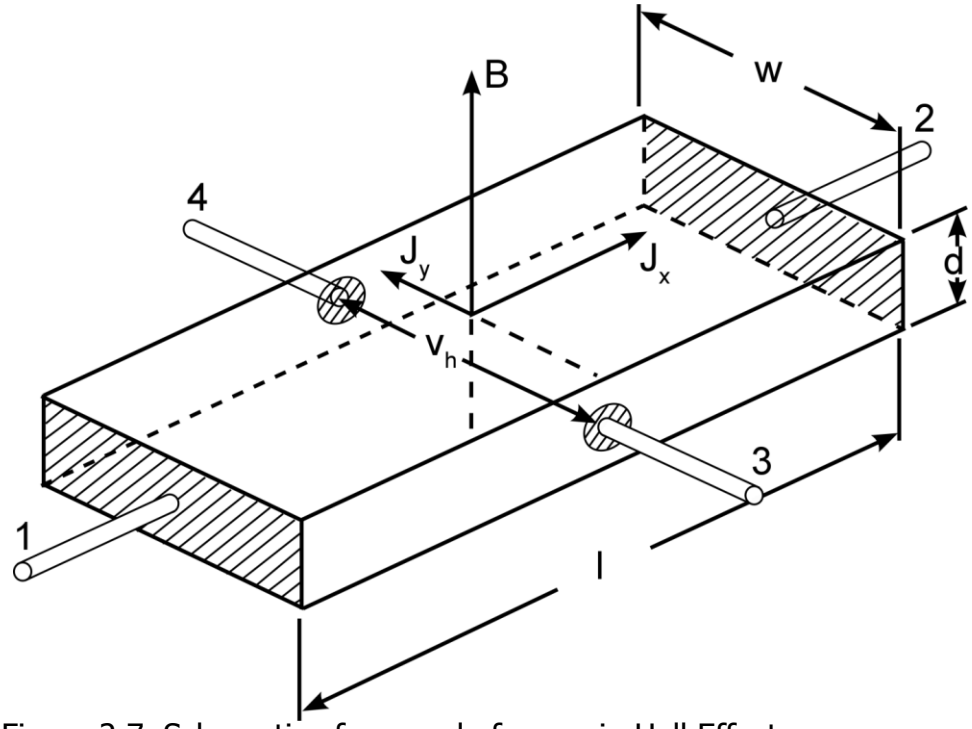

Figure 2.7. Schematic of a sample for use in Hall Effect measurements.

measured between the Hall electrodes for $B \neq 0$ is the algebraic sum of the misalignment potential and of the Hall voltage. This misalignment potential can be eliminated by measuring V for opposite magnetic orientations of the magnetic field (normal to the film surface) and current, while holding all other parameters constant. A typical magneto-transport experimental setup is shown in Figure 2.9.[82]

Optical Characterization

The most direct and method for probing the band structure of semiconductors is to measure the absorption spectrum. In the absorption process, a photon of a known energy excites an electron from a lower to a higher energy state.[67]

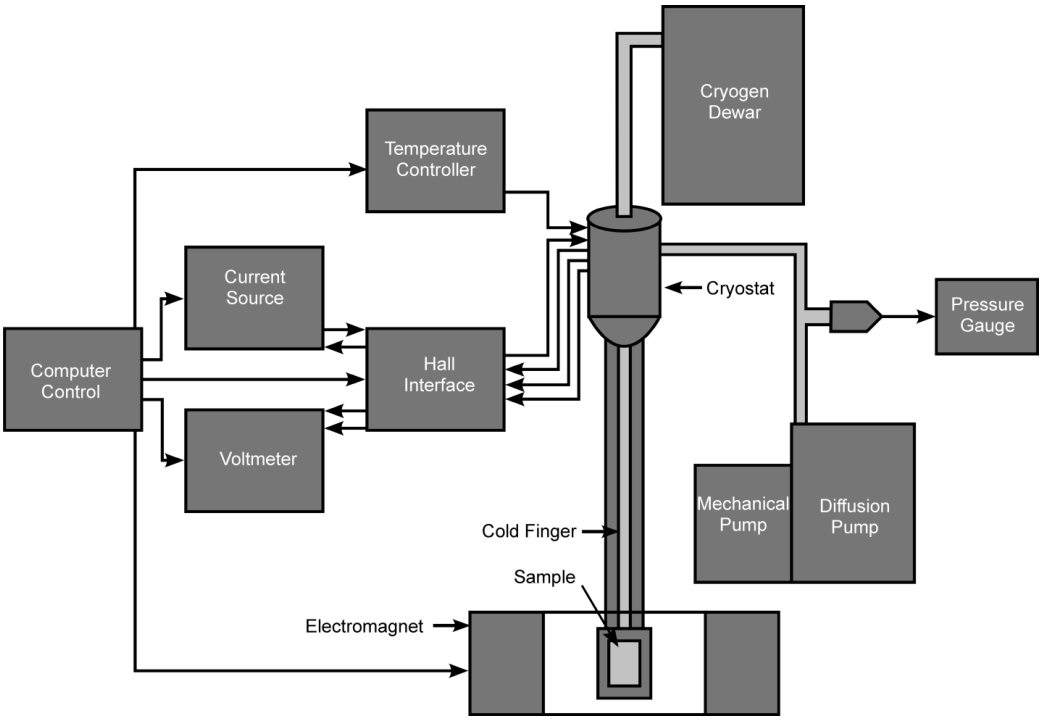

Figure 2.8. Experimental setup for Hall effect measurements.

Placing a semiconductor at the output of a monochromator and studying the reduction in the transmitted radiation, can express all the possible transitions an electron can make and learn much about the distribution of states.[67] The fundamental absorption that is typically observed includes all transitions of an electron from the valence band to the conduction band. The fundamental absorption, which manifests itself by a rapid rise in absorption, can be used to determine the energy gap of the semiconductor.[67] The momentum of a photon, h/λ, is very small compared to the crystal momentum, h/a, therefore the photon-absorption process should conserve the momentum of the electron.[67] The absorption coefficient $\alpha(h\nu)$ for a given photon energy $h\nu$ is proportional to the probability P_{if} for the transition from the initial to the final state and to the density of states of electrons in the initial state, n_i, and also the

density of available empty final states, n_f, and this process must be summed for all possible transitions between states separated by an energy difference equal to $h\nu$ [67]:

$$\alpha(h\nu)=A\Sigma P_{if}n_i n_f$$

In the following derivation, by Pankove [67] it is assumed that all the lower states are filled and that all the upper state are empty, a condition which is true for an undoped semiconductor at 0 K. For an absorption transition between two direct valleys where all the momentum-conserving transitions are allowed, i.e., the transition probability P_{if} is independent of photon energy. Every initial state at E_i is associated with a final state such that:

$$E_f=h\nu-E_i$$

But in parabolic bands,

$$E_f-E_g=\hbar^2k^2/2m_e$$

where E_g is the energy gap and

$$E_i=\hbar^2k^2/2m_e$$

Therefore,

$$h\nu - E_g = h^2k^2/2(1/m_e+1/m_h)$$

The density of directly associated states can then be found as

$$N(h\nu)d(h\nu)=8\pi k^2dk/(2\pi)^3=(2m_r)^{3/2}/2\pi^2h^3\,(h\nu-Eg)^{1/2}d(h\nu)$$

where m_r is the reduces mass given by $1/m_r = 1/m_e$. Hence the absorption coefficient is

$$\alpha(h\nu)=A(h\nu-Eg)^{1/2}$$

where A is given by

$$A=q^2(2m_hm_e/m_h+m_e)^{3/2}/nch^2m_e$$

A plot of the square of α($h\nu$) as a function of photon energy near the fundamental absorption edge will result in the straight line in the case of the direct transition.[67]

The absorbance is measured as a peak height and defined as the logarithm of the ratio of the spectral radiant intensity, I_0, of incident, essentially monochromatic light, to the spectral intensity of the transmitted radiation, I , i.e., $A = log\ (I_0/I)$. This definition supposes that all the incident light is either transmitted or absorbed, reflection or scattering being negligible. In general, the absorption coefficient can be obtained from the Lambert-Beer law, which states that the attenuation of the light beam traveling through a light absorbing medium is described by equation $I = I_0\ e^{-ax}$, where I is the intensity of the transmitted beam, I_0 is the intensity of the incident beam, a is the absorption coefficient of the medium and x is the length of the light path in the sample or the thickness of the sample.

CHAPTER 3

GROWTH AND CHARACTERIZATION OF β-$FeSi_2$ AND β-$Fe(SiGe)_2$

Properties of β-$FeSi_2$

Except for a preliminary report of faint luminescence from ion-beam synthesized osmium silicide precipitates,[83] β-$FeSi_2$ is the only transition metal silicide to demonstrate light emission. This along with β-$FeSi_2$ having inexpensive and abundant constituent elements has therefore attracted considerable attention as a possible technological solution to the lack of a silicon-based light emitting material which can be cheaply integrated with current VLSI devices and transmission through optical fibers.

This represents an effort funded by the Office of Naval Research to determine the tenability range of the alloy β-$Fe(SiGe)_2$ as grown by molecular beam epitaxy as well as the alteration of the band gap due to germanium incorporation as measured by Fourier transform infrared spectroscopy.

Phases and Crystal Structure

$FeSi_2$ occurs in two thermodynamically stable phases, a metallic phase (α) and a semiconducting phase (β).[34] The semiconducting β-$FeSi_2$ has an orthorhombic crystal structure and belongs to the *Cmca* space group.[84] The standard orthorhombic cell (a = 0.98 nm, b = 0.780 nm, c = 0.783 nm) contains 48 atoms which can be described as the CaF_2 structure after a Jahn-Teller distortion.[85] The primitive cell contains 24 atoms, of which 8 iron and 16 silicon atoms can be grouped into two equal sets (Fe1, Fe2, Si1, Si2) of crystallographically inequivalent sites with slightly different

distances.[34] The atomic positions within the primitive unit cell are listed in Table 3.1. The projection of the unit cell onto the a-c plane is shown in Figure 3.1.[86]

Table 3.1. Atomic positions (in units of the primitive translation vectors) in β-$FeSi_2$.

Atom	Site	X	Y	Z
Fe1	8d	0.21465	0.0	0.0
Fe2	8f	0.0	0.19139	0.81504
Si1	16g	0.37177	0.27465	0.44880
Si2	16g	0.12729	0.04499	0.27392

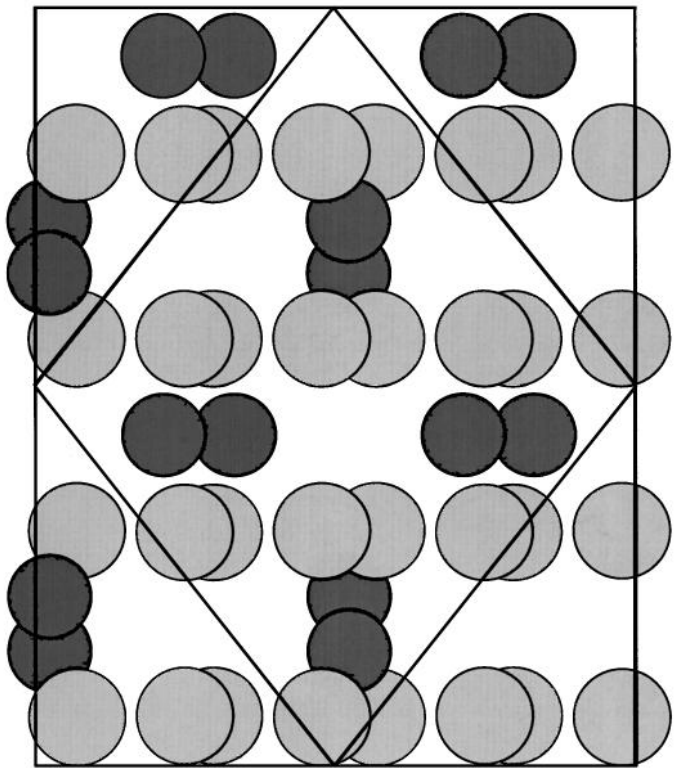

Figure 3.1. Project of atomic positions (light: Si: dark: Fe) on the a-c plane of the simple orthorhombic unic cell of β-$FeSi_2$. Also shown are the lattice vectors (a+c)/2 and (a-c)/2 for the one-face centered unit cell [34].

The β-$FeSi_2$ semiconducting phase transitions into the metallic α-$FeSi_2$ at 937°C which has a tetragonal crystal structure.[87] Of the transition metal silicides, $FeSi_2$ is the only one reported to occur in both metallic and semiconducting phases which is a desirable trait for device processing as interconnects may be produced through localized heating.

Orthorhombic β-$FeSi_2$ acceptably matches Si(001) and Si(111) substrates.[34] β-$FeSi_2$(100) growth on Si(100) orients itself in two possible orientations rotated by 45° azimuthally as shown in Figure 3.2. The orientations are β-$FeSi_2$[010]||Si<110> (A-type) and β-$FeSi_2$[010]||Si<100> (B-type) with areas of 0.61 and 1.22 nm^2 respectively. The A-type has a mismatch of 2% and the B-type has a mismatch of -4%, making the A-type orientation more preferential to growth.[34] β-$FeSi_2$ is highly sensitive to its lattice parameters and therefore to the orientation at which the material is grown on silicon. The A-type orientation has been shown to be more favorable to a direct band gap.[88]

$FeGe_2$ has not been observed in the β phase experimentally. However, Tani and Kido theoretically considered alloying β-$FeSi_2$ with the hypothetical β-$FeGe_2$ and determined that an increase in Ge results in a decrease of the direct band gap.[89] There has been a report of semiconducting Ge–Si–Fe alloy thin film grown on Si(100) by reactive deposition epitaxy.[90] This was accomplished by deposition of an iron film on a SiGe/Si(100) structure, then the alloying with an annealing process. They reported that the alloyed film can be regarded as distorted β-$FeSi_2$ due to participation of germanium with a reported stoichiometry of $FeSi_{1.92}Ge_{0.08}$. From optical measurements,

this resulted in direct band gap of 0.83 eV, a shift from the 0.87 eV typically observed, indicating a redshift of the band gap with regard to that of β-$FeSi_2$. Further, Murakami *et al.* reported solid phase growth of [a-SiGe/β-$FeSi_{2-x}Ge_x$]$_n$ layered structures which, following annealing resulted in β-Fe($Si_{1-x}Ge_x$) films with x as large as 0.07.[91] However, Ge segregation occurred when x=0.1.

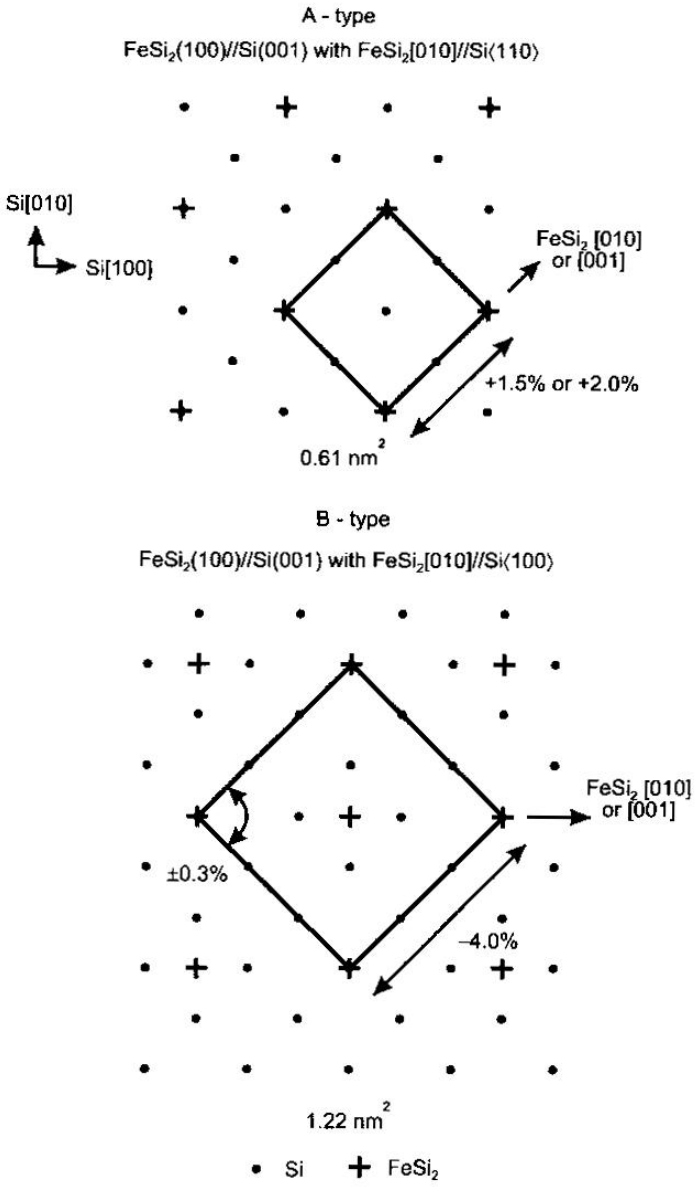

Figure 3.2. Lattice matching of β-$FeSi_2$ to Si(001).

Electronic Properties of β-$FeSi_2$

The room temperature carrier concentration in β-$FeSi_2$ ranges from 10^{18} to 10^{19} cm^{-3} for polycrystalline films and one or two orders of magnitude lower in single crystals.[34] The carrier mobilities are typically on the order of 10 $cm^2/V \cdot s$ at room temperature.[92, 34] Although these are less than ideal electronic properties, β-$FeSi_2$ light emission at 1.5 um has resulted in resurgence of research interest.

The complex band structure of β-$FeSi_2$ has elicited significant debate as to the exact nature of the band gap. The band gap has been described as quasi-direct due to many experimental reports of both indirect and direct gap behavior.[93-99] Extensive theoretical work has been performed on β-$FeSi_2$ and, independent of methodology, trends within the Brillouin zone can be reliably predicted.[100] Further, certain types of strain have been shown to possibly tailor the nature of the gap.

The Brillouin zone is shown in Figure 3.3 with labels on points of high symmetry.[101] Linear muffin-tin orbital (LMTO) calculations performed by Filonov *et al.* [101] resulted in the band structure shown in Figure 3.4. There are a total number of 128 valence electrons per unit cell, and the band gap appears between the 64^{th} and 65^{th} bands. There are three direct gaps within a small energy range, but the conduction band at the Y point is only 8 meV higher than at the Λ point, making the gap nature difficult to define.[101] The conduction band in the vicinity of the Λ point is almost flat along many other directions within the Brillouin zone, thus leading to indirect gaps.[100] Table 3.2 lists the eigenvalues of the valence band maxima and conduction band minima at some of the high points of symmetry.

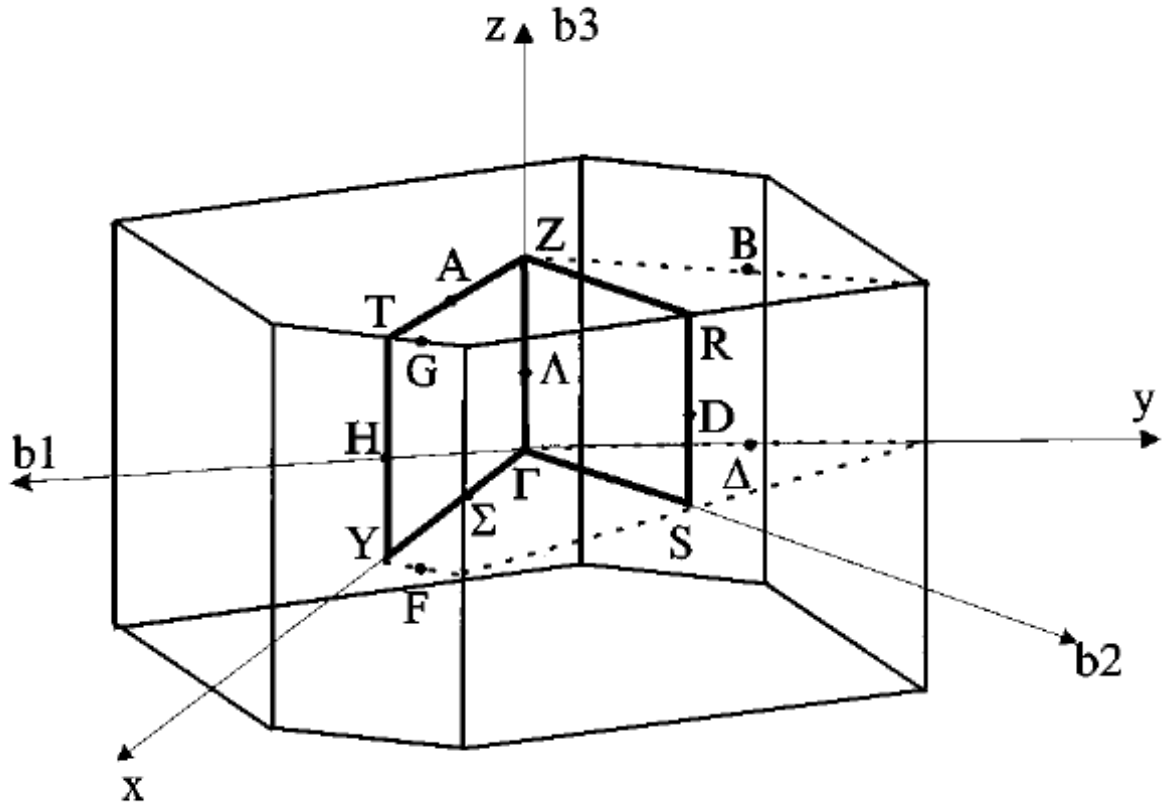

Figure 3.3. Brillioun zone for the base-centered orthorhombic structure. The irreducible part is marked by broken lines.

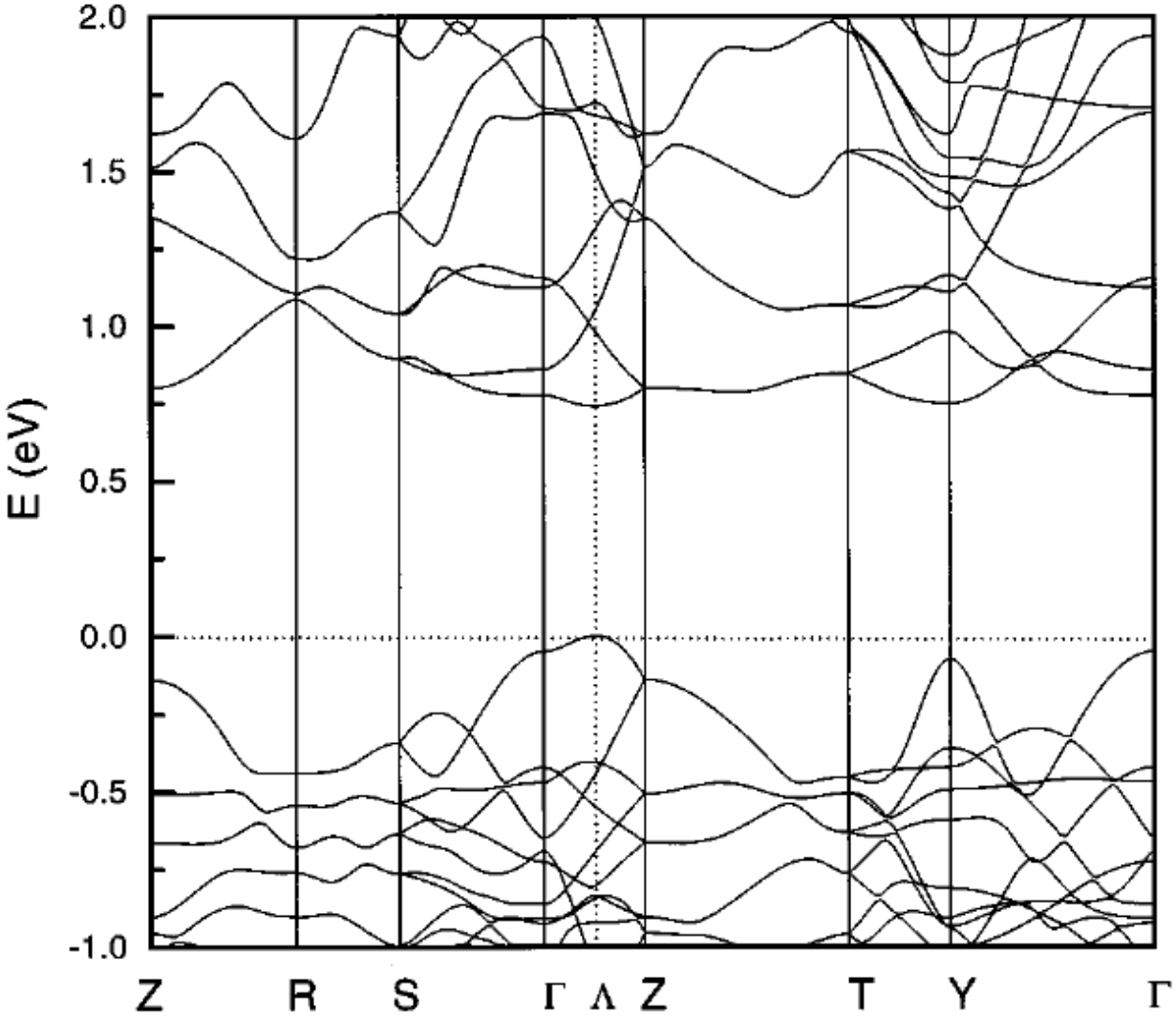

Figure 3.4. Band structure of β-$FeSi_2$ along the standard contour.[100]

Table 3.2. Eigenvalues in eV of the top of the valence and bottom of the conduction bands at some high symmetry points of the Brillouin zone. [100]

	Γ	Y	Λ	Λ-H	Λ-G	Λ-T
E_v	-0.050	-0.075	0.0	0.0	0.0	0.0
E_c	0.778	0.750	0.742	0.738	0.741	0.740

Filonov *et al.* [101] also calculated the dependence of the total and projected densities of states on energy which is shown in Figure 3.5. The valence band extends down to about -13.5 eV below the Fermi energy, and can be divided into three main parts. The first part is from the bottom up to about -7.0 eV and corresponds to pure Si *s*-like states. The second wide region is from -7.0 eV up to about -2.0 eV where bonding Si-*p* and Fe-*d* states play a dominant role. The third part starts at -2.0 eV and can be characterized as the region of nonbonding Fe-d states. These results are in good agreement with other theoretical calculations and experimental data.[93,102]

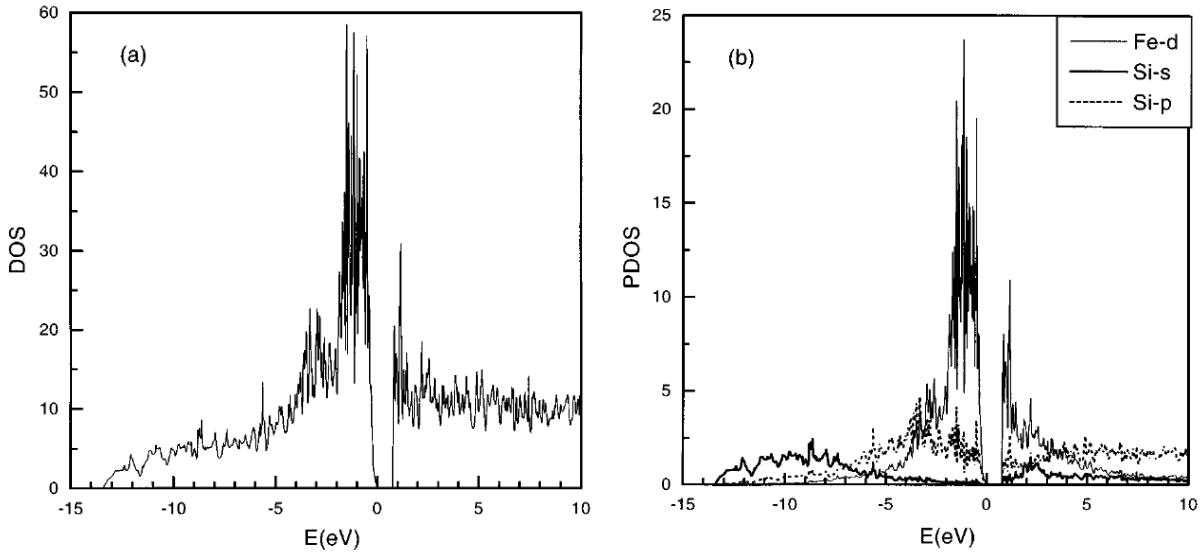

Figure 3.5. (a)Total and (b) projected density of states for β-$FeSi_2$. The zero on the energy scale corresponds to the top of the valence band. [100]

Previous Growth of β-$FeSi_2$

A significant effort has been carried out on the growth of single crystal β-$FeSi_2$. Wandji *et al.*[103] first demonstrated single crystal growth using I_2 as a transport agent resulting in crystals up to 3mm in length. High purity β-$FeSi_2$ crystals with good

structural perfection were grown using chemical vapor transport.[104] Doping of single crystal β-$FeSi_2$ was achieved using cobalt and nickel (n-type) and chromium and manganese (p-type). The doped crystals were larger and the transport rates higher.[34]

A wide range of growth techniques have been employed to produce β-$FeSi_2$ thin films, including sputtering and evaporation of iron onto silicon followed by annealing, codeposition of the constituent elements on room temperature or heated silicon, cosputtering or laser ablation from composite targets of similar composition, and ion implantation forming buried layers. These methods have synthesized both poly crystalline and epitaxial films of $FeSi_2$ on Si(001) and (111).[34] Codeposition has produced higher quality films than iron deposition due to the latter requiring growth to proceed through a phase sequence from metal-rich toward Si-rich by a long-range diffusion process of metal or silicon through the already form layer of silicide.[34]

Self-assembly of nanostructures may help to overcome the resolution limitations of conventional lithography for device applications.[105] In this effort, nanostructures of β-$FeSi_2$ have been recently demonstrated with increasing crystalline quality and control of self-assembly. Epitaxial β-$FeSi_2$ nanodots were grown on strained $Si/Si_{0.8}Ge_{0.2}$ (001) substrates by solid phase epitaxy method.[106] The high quality of the nanodots was attributed to a decrease of the in-plane lattice mismatch between the lattice parameters of the β-FeSi2 [001] and [010] directions and that of Si substrate.[106] Nakamura *et al.* demonstrated the formation of β-$FeSi_2$ nanodots by codeposition at disilicide stoichiometric deposition rates on Si(111) substrates covered with ultrathin

SiO_2 films.[107] These were shown to be hemispherical nanodots with ultrahigh density (10^{12} cm^{-2}) and a narrow size distribution with an average diameter of 5 nm.

Interestingly $FeSi_2$ nanodots have been found to act as a catalyst for the growth of carbon nanotubes and $TaSi_2$ nanowires. Using chemical vapor deposition with $FeSi_2$ as a catalyst, double walled carbon nanotubes (DWNT) with narrow diameter distribution were demonstrated.[108] The as-produced materials showed DWNT diameters of 4.5±0.5 nm which was attributed to using $FeSi_2$ as a catalyst. $TaSi_2$ nanowires have were synthesized by annealing $FeSi_2$ thin films and nanodots grown on a Si substrate in an ambient containing Ta vapor.[109] The $TaSi_2$ nanowires were formed in three steps; segregation of Si atoms from the $FeSi_2$ underlayer to form Si base, growth of $TaSi_2$ nanodots on Si base, and elongation of $TaSi_2$ nanowire along the growth direction. The length of nanowires ranges from several hundreds of nanometers to several micrometers and the diameters of the nanowires are about 20–40 nm.[109]

Single-crystalline FeSi free-standing nanowires were grown from a *trans*-$Fe(SiCl_3)_2(CO)_4$ single-source precursor using chemical vapor deposition with no intentional metal catalyst.[110] Room-temperature electrical transport measurements using NW devices show an average resistivity of 210 μΩcm, similar to the value for bulk FeSi.

Reports of Light Emission

A light-emitting diode (LED) based on ion beam synthesized β-$FeSi_2$ was reported by Leong *et al.*[111] This LED was fabricated by high dose ion implantation into a

silicon substrate followed by annealing. It demonstrated ~1.5 um electroluminescence at room temperature. This created considerable excitement, but questions immediately arose as to the origin of the luminescence since significant light emission had not been achieved in β-$FeSi_2$ grown by methods other than ion-beam synthesis.

Hunt *et al.* reported photoluminescence from ion-beam synthesized β-$FeSi_2$ but found the luminescence disappeared with the β-α transition, providing strong evidence that the PL signal arises from the disilicide.[112] Radermacher *et al.* suggest, however, that this PL could be due to structural defects in the Si substrate, particularly the D1 dislocation which emits at 0.81 eV.[113,114] More recently, Grimaldi *et al.* and Spinoza *et al.* performed a number of experiments to disentangle the contribution to the 1.55 μm luminescence of the β-$FeSi_2$ from that of the Si defects.[115,116,100] These support the argument that the PL is intrinsic to the β-$FeSi_2$ precipitates. Further, Birdwell's photoreflectance study of β-$FeSi_2$ precipitates provide evidence that the observed light emission originates from the disilicide, and that stress makes it possible.[100]

Spinella *et al.* found that the carrier recombination within iron precipitates produced by IBS was characterized by a weak oscillator strength resulting in a decay lifetime of the 1.54 μm signal of ~60 μs (at 17 K).[117] Schuller *et al.* performed time resolved-PL measurements on IBS grown precipitates and, similarly, found a long decay time of 10 μs at 10 K and a low quantum efficiency, indicative of an indirect bandgap.[118] Conversely, the β-$FeSi_2$ LED device they measured showed a fast time response of <30 ns at 20 K.

A double heterostructure of Si/β-$FeSi_2$/Si was produced by MBE which demonstrated 1.55 μm photoluminescence at low temperatures.[119] Time-resolved PL measurements elucidated that the luminescence originated from two sources, one with a short decay time (τ~10 ns) and the other with a long decay time (τ~100 ns).

In an investigation into the nature of the band gap of β-$FeSi_2$, photoreflectance (PR) spectra were obtained from an epitaxial film and a bulk single crystal of β-$FeSi_2$ at low temperatures (T<180 K) by Birdwell *et al.*[120] From the analysis of the spectra taken on the thin film, the free exciton binding energy was found to be 0.009±0.002 eV and a direct energy gap of 0.934±0.002 eV at 0 K. The MBE film spectrum showed other weak features which can be attributed to an impurity transition at 0.904 eV and bound exciton transition at 0.914 eV.[120] The redshift of the direct transitions of the MBE film relative to the single crystal strongly suggest that the surface of the epitaxial film is under tensile stress. Very recently, Birdwell *et al.* examined the PR spectra obtained from an MBE grown film and a single crystal of β−$FeSi_2$.[121] They report an additional weaker resonance at even lower energies which was found to be composed of phonon-assisted indirect transitions involving the ground and first excited state of the free exciton. This indirect gap of the MBE grown film was determined to be 0.823±0.002 eV at 75 K.

Experimental Study

Double side polished, 500 μm thick, Si(100) (±0.25°) wafers were prepared using the Shiraki method discussed in Chapter 2. The wafers were then mounted on a Mo sample holder, affixed by Mo clips. This sample holder was inserted into the load

lock of an ultrahigh vacuum deposition chamber (background pressure on the order of 10^{-11} Torr) and then mechanically transferred to and mounted on the substrate manipulator and heater within the main deposition chamber. Reflection high-energy electron diffraction (RHEED) performed on the as inserted wafer demonstrated a blurred image superimposed on a streaked Si(100) diffraction pattern with a (2x1) reconstruction. The wafer was then exposed to a low Si flux (< 1 Å/s) while heated to 800°C resulting in a removal of the oxide as demonstrated by the RHEED patterns distinct transition to a purely Si(100) 2x1 reconstruction.

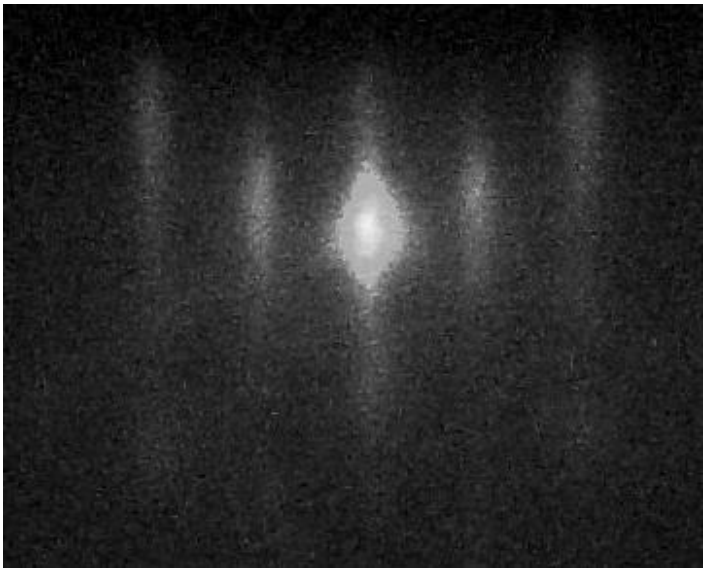

Figure 3.6. 2x1 reconstructed Si buffer layer.

A 50-100 nm Si layer was grown (Si flux of 1 Å/s) on top of each cleaned substrate with a substrate temperature (Ts) of 400-500°C. A representative RHEED image for this Si buffer layer is shown in Figure 3.6.

Several monolayers of stoichiometric Fe and Si (Fe:Si::1:2) were deposited, Ts=600 °C. This was followed by a ~5 min anneal at 800 °C forming a β-$FeSi_2$ template

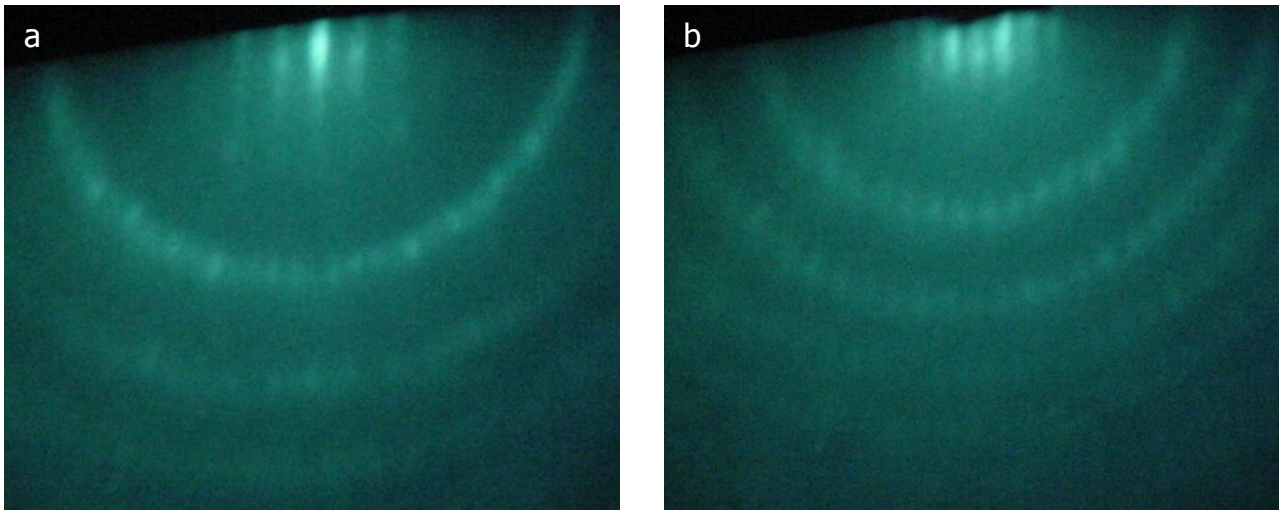

Figure 3.7. β-$FeSi_2$ RHEED streaks obtained during growth along: (a) β-$FeSi_2$(100) and (b) β-$FeSi_2$(110) directions.

layer as evidenced by the collected RHEED images. In Figure 3.7, the observed template layer diffraction patterns are identified according their axial orientation to the Si substrate. The patterns are similar to those typically seen during previous growth studies of the beta phase of $FeSi_2$.[122] The streaked patterns indicate two dimensional growth is occurring.

Finally, for epilayer growth, appropriate Fe, Si, and Ge fluxes (Fe:Si:Ge = 1:2−2x:2x) are established, and growth continued (Ts and r unchanged) until a film of ~500nm was obtained. The Ge concentrations and thicknesses indicated were determined by Rutherford backscattering (RBS) and X-ray diffraction (XRD).

Rutherford Backscattering Spectroscopy

Backscattered particles are detected with a detector operated which operates like

a solid state diode under reverse bias. The applied high voltage generates a thick depletion layer and any charge created by the radiation in this layer is collected at an electrode.[123] The charge collected is proportional to the energy deposited in the detector allowing the devices to yield information about the energy.

The signal from the detector is amplified and analyzed with a multi-channel pulse height analyzer (PHA). A computer interface module is used to plot counts as a function of channel number, which represents energy.

Channeling is a phenomenon that occurs in single-crystal samples when the ion beam is incident along or near a major crystallographic direction.[123] Correlated, small-angle collisions with the atoms in the atomic rows or planes lead to very regular oscillations of the ion trajectory within the lattice. As a result, the backscattering yield for channeled ions is reduced over that for ions moving randomly within the lattice.

Since any atom displaced from a lattice site into the interstitial space will interact strongly with channeled ions, ion channeling can be used for structural characterization including profiling of defects and lattice strain, and lattice-location of impurities (i.e., interstitial or substitutional impurities).

RBS was performed using a 1.5 MeV He+ beam at a scattering angle of 135° and a detector resolution of 19 keV. RBS spectra (channeled, random, and simulated) from a β-$FeSi_2$ epilayer are shown in Fig. 3.8. The ratio of channeled to random yield is 0.14 indicating high crystalline as well as a slightly iron rich $FeSi_2$ stoichiometry (Fe:Si::1.08:2). From the RBS spectra for a series of Fe-Si samples, the effusion cell

and e-beam evaporator flux rates were calibrated and proper stoichiometry was achieved. Further, the simulated data provided film thicknesses.

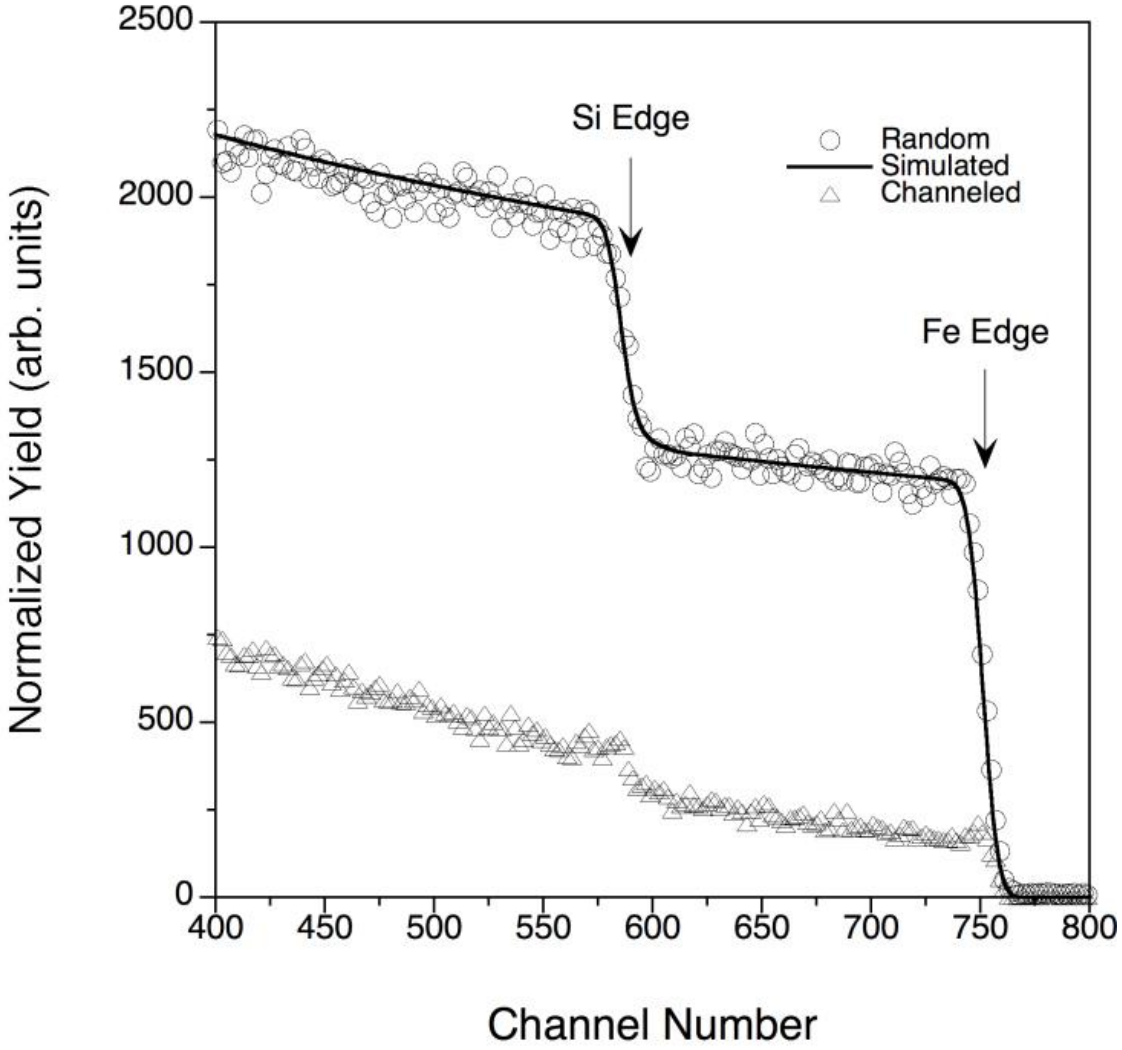

Figure 3.8. RBS spectra from 500 nm β-FeSi2 epilayer, Tsub=700°C, with a random to channeled yield ratio of ~14% indicating a high crystalline quality.

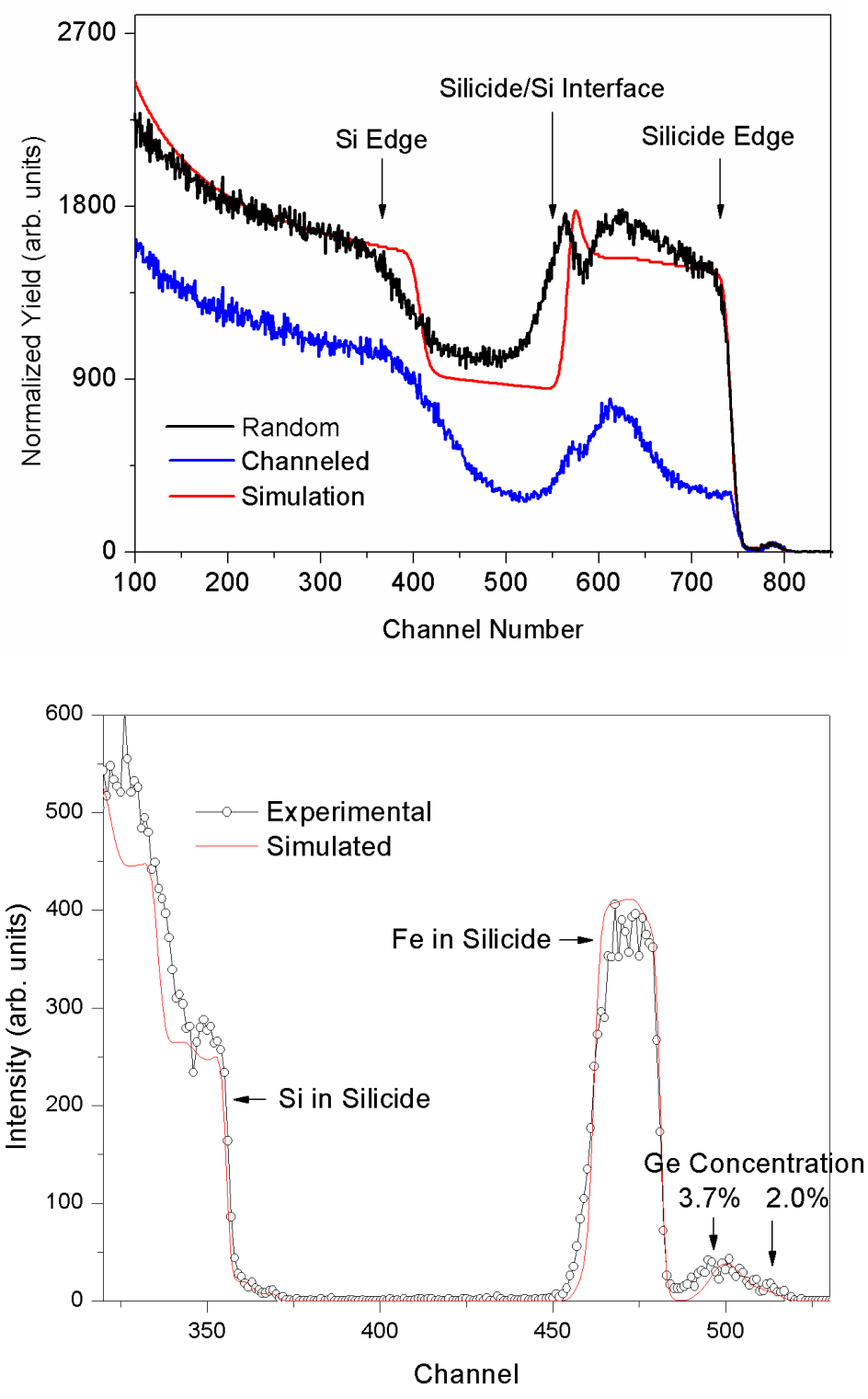

Figure 3.9. RBS spectrum for $Fe(Si_{1-x}Ge_x)_2$ for (a) x=0.005 plotted, showing channeling and simulated results and (b) x=0.04 epilayer, showing low Ge uniformity, typical for samples with $x \geq 0.04$.

RBS measurements of $Fe(Si_{1-x}Ge_x)_2$ samples were performed for samples for nominal values of x ranging from 0.005 to 0.15. RBS spectra are shown in Figure 3.9 (a) and (b) for 0.5% Ge and a nominal 4% Ge respectively. It was found that for x=0.005, the channeled to random yield ratio remained low (~0.20), indicating still fairly high crystallinity. For x > 0.04, Ge segregation from the film occurred as shown in Figure 3.10. This demonstrates a miscibility range similar to that seen previously by solid-phase epitaxy and reactive deposition epitaxy.[90,91]

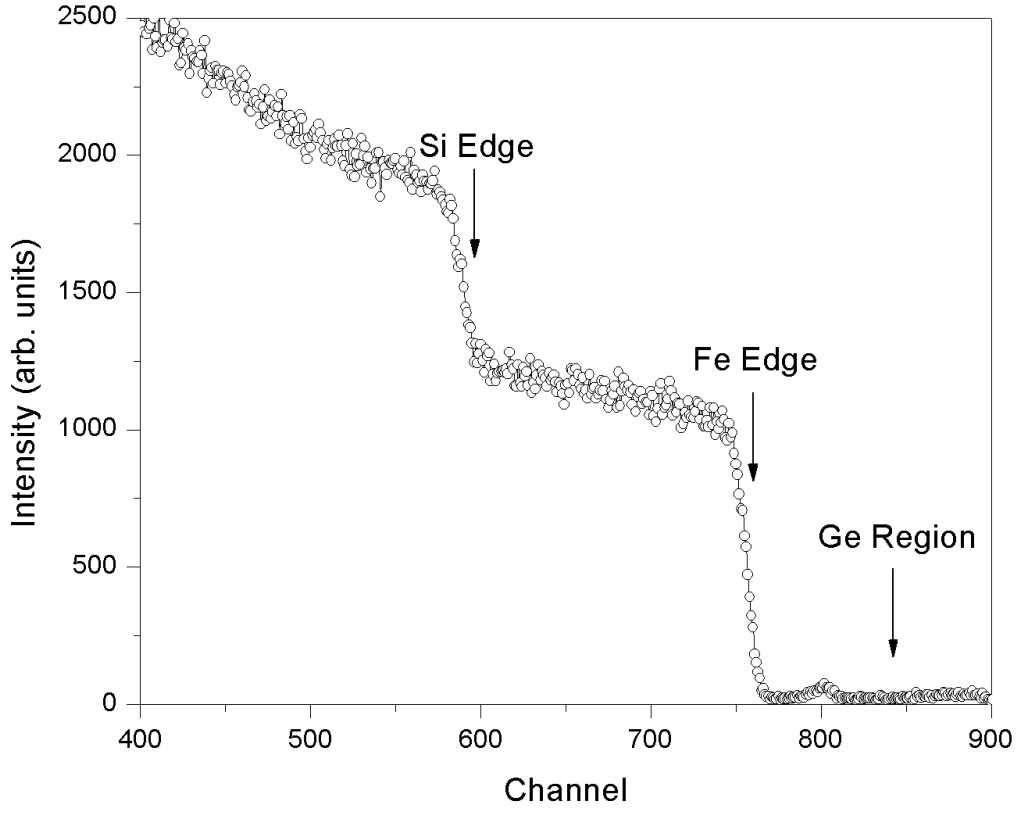

Figure 3.10. RBS spectrum for $Fe(Si_{1-x}Ge_x)_2$ for x=0.15. The Ge region marked can only be simulated by use of a Ge surface layer, suggesting Ge has segregated to the surface of the film.

X-Ray Diffraction

In order to determine the phase, orientation, thickness, and crystallinity of the Fe-Si-Ge samples, out-of-plane XRD measurements were performed using a four-circle Huber diffractometer mounted at a rotating anode with a copper target and a maximum power of 12 kW. A flat Ge(2 2 0) monochromator at wavelength 1.5406 Å was used for data analysis in the [0 0 1] direction of the Si substrate. XRD spectra for the β-$FeSi_2$ and nominally β-$Fe(Si_{0.85}Ge_{0.15})_2$ are shown in Figures 3.11 (a) and (b), respectively. For the pure silicide, the measured peak of $2\theta = 36.424°$ corresponds to a lattice parameter of 9.862 Å, in, close agreement with the accepted bulk for the β-phase (100) direction unstrained value of 9.863 Å. In the sample with a nominal 15% Ge concentration, the lattice parameter is found to be 9.870 Å, which most closely fits a tensile strained β-phase (100) direction. This increase in lattice parameter corresponds to the change Tani and Kido predicted for 6% Ge incorporation.[89] However, a significant Ge peak is seen at $2\theta = 67.329$, indicating major segregation of the Ge and offering an explanation for the discrepancy from the expected 15% Ge concentration and in agreement with the segregation seen in the RBS spectrum for this sample. Similar segregation is seen in all samples with $x>0.04$.

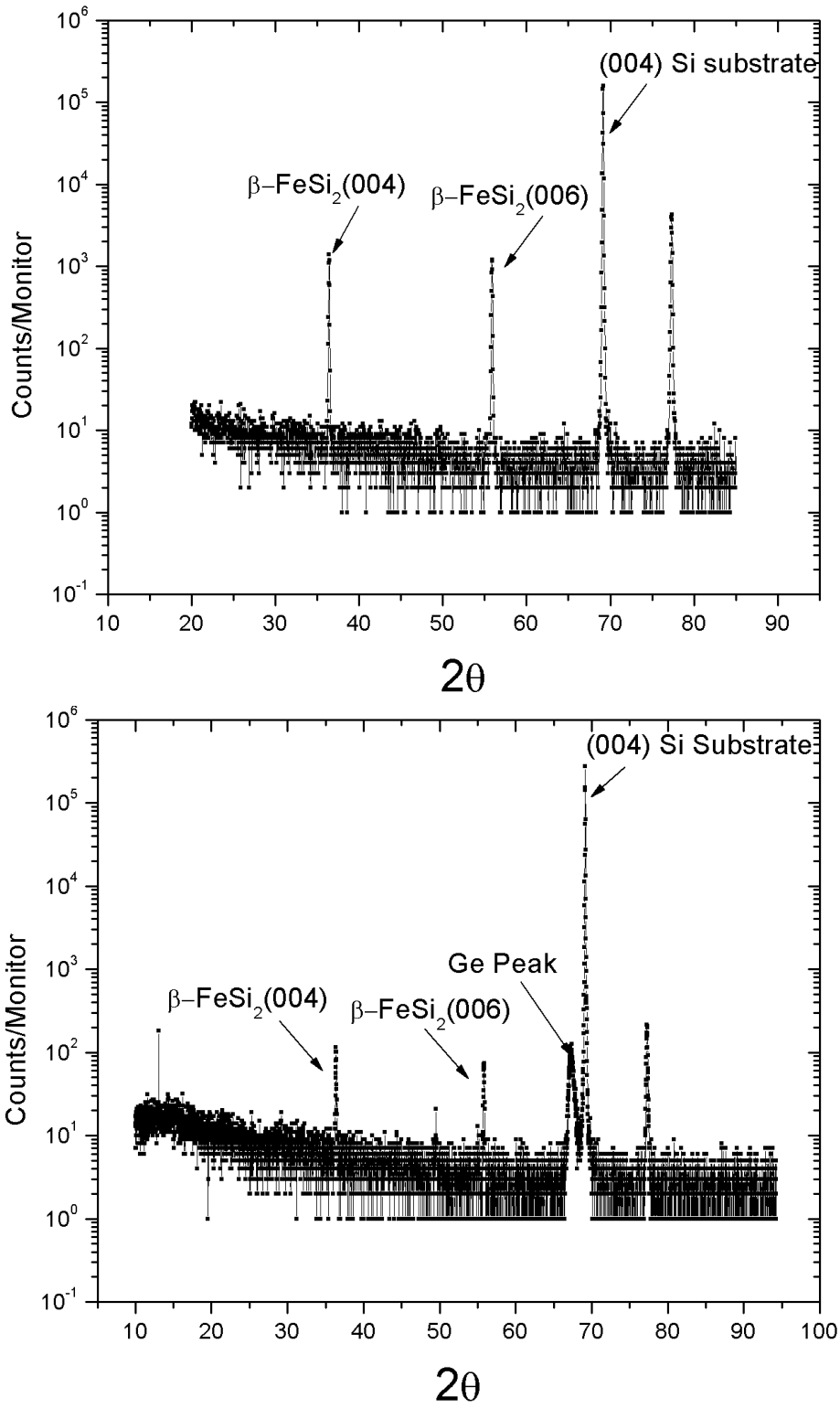

Figure 3.11. XRD spectra of (a) pure $FeSi_2$ with lattice constant equal to the (100) direction of the semiconducting β phase and (b) nominally $Fe(Si_{1.85}Ge_{0.15})_2$ demonstrating a tensile strained (100) orientation of the β phase with significant Ge segregation.

FTIR Absorption Spectroscopy

Tani and Kido theoretically considered alloying β-$FeSi_2$ with the hypothetical β-$FeGe_2$ and determined that an increase in Ge results in a decrease of the direct band gap.[89] Chen *et al.*[90] and Murakami *et al.*[91] experimentally produced the alloy by reactive deposition epitaxy and solid-phase growth, respectively. Chen reported that optical transmission of the silicide/germanide alloy shows a band gap reduction with respect to the pure silicide, 0.87–0.83 eV, for a germanium fraction of x=0.03. Murikami reported that Ge doping results in 0.4%–0.5% strain due to both Ge incorporation and segregated SiGe nanocrystals.

As MBE affords more control since it is not bound by equilibrium conditions, it makes for a useful study to determine the how the energy gap of MBE grown samples is affected by the addition of Ge. The results of an investigation into the variation of E_g with temperature in a series of β-$Fe(Si_{1-x}Ge_x)_2$ epilayers that span a range of nominal alloy compositions ($0 < x < 0.15$) are presented.

FTIR spectroscopy was performed at 4 K and room temperature using a white light source and a DTGS detector between 2500 and 10,000 wavenumbers. A plain Si wafer was used as a background. The energy gap, Eg, at each temperature was determined, assuming a parabolic band structure, from extrapolation of the slope of the absorption coefficient squared versus the photon energy to the baseline (where the square of the absorption coefficient equals zero).

Plotted in Figure 3.12 is the absorption coefficient squared for the pure β-$FeSi_2$ sample at room temperature (RT) and 4 K. The linear fit of the fundamental absorption

region approximates the direct band gap values to be 0.86 and 0.91 eV for RT and 4K respectively. The RT value is somewhat lower than Rebien *et al.* who report on the direct band gap value for β-$FeSi_2$ epitaxial films to be 0.89 and 0.93 eV for RT and 10K respectively.[124] It does fit in with the general range (0.84 to 0.90 eV at RT) reported from most absorption studies.[34] Another section of the RT spectrum can be fitted to a linear curve with a y-intercept of 0.81 eV, possibly due to silicon or film defects.

Fabry-Pérot interference fringes are apparent at energies below the absorption edge. Further confirmation of the epitaxial layer thickness was obtained from the fringe spacings, where the layer thickness t is given by the relationship

$$t = \lambda_1\lambda_2(m_1 - m_2)/2(n_1\lambda_2 - n_2\lambda_1)$$

where λ_1 and λ_2 are the wavelength maxima (or minima), m_1 and m_2 are integers corresponding to the orders of the fringes, and n_1 and n_2 are the refractive indices of the β-$FeSi_2$ alloy at λ_1 and λ_2, respectively. The calculated thickness was 760 nm.

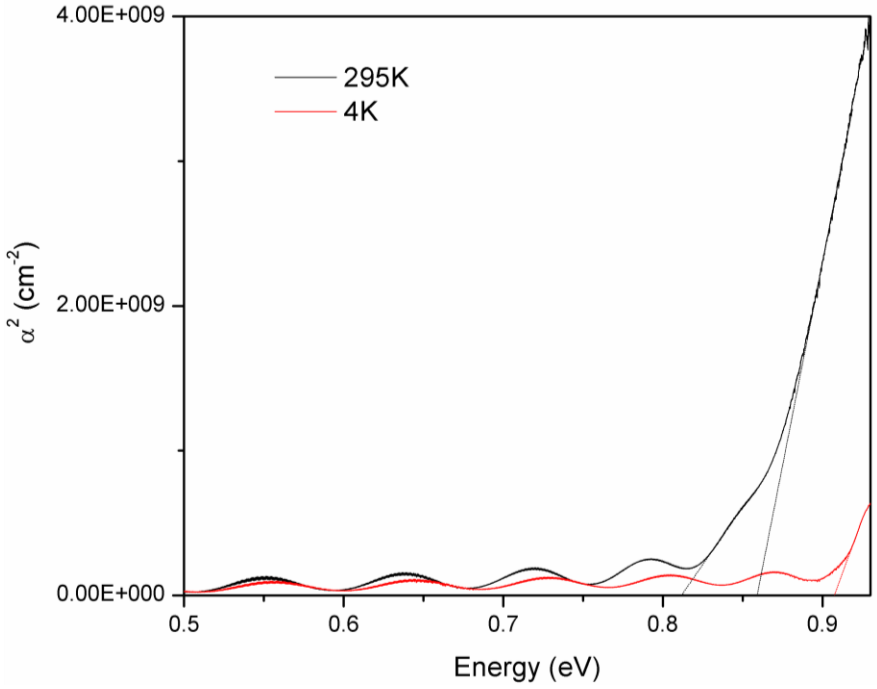

Figure 3.12. Absorption coefficient squared vs. photon energy for β-$FeSi_2$.

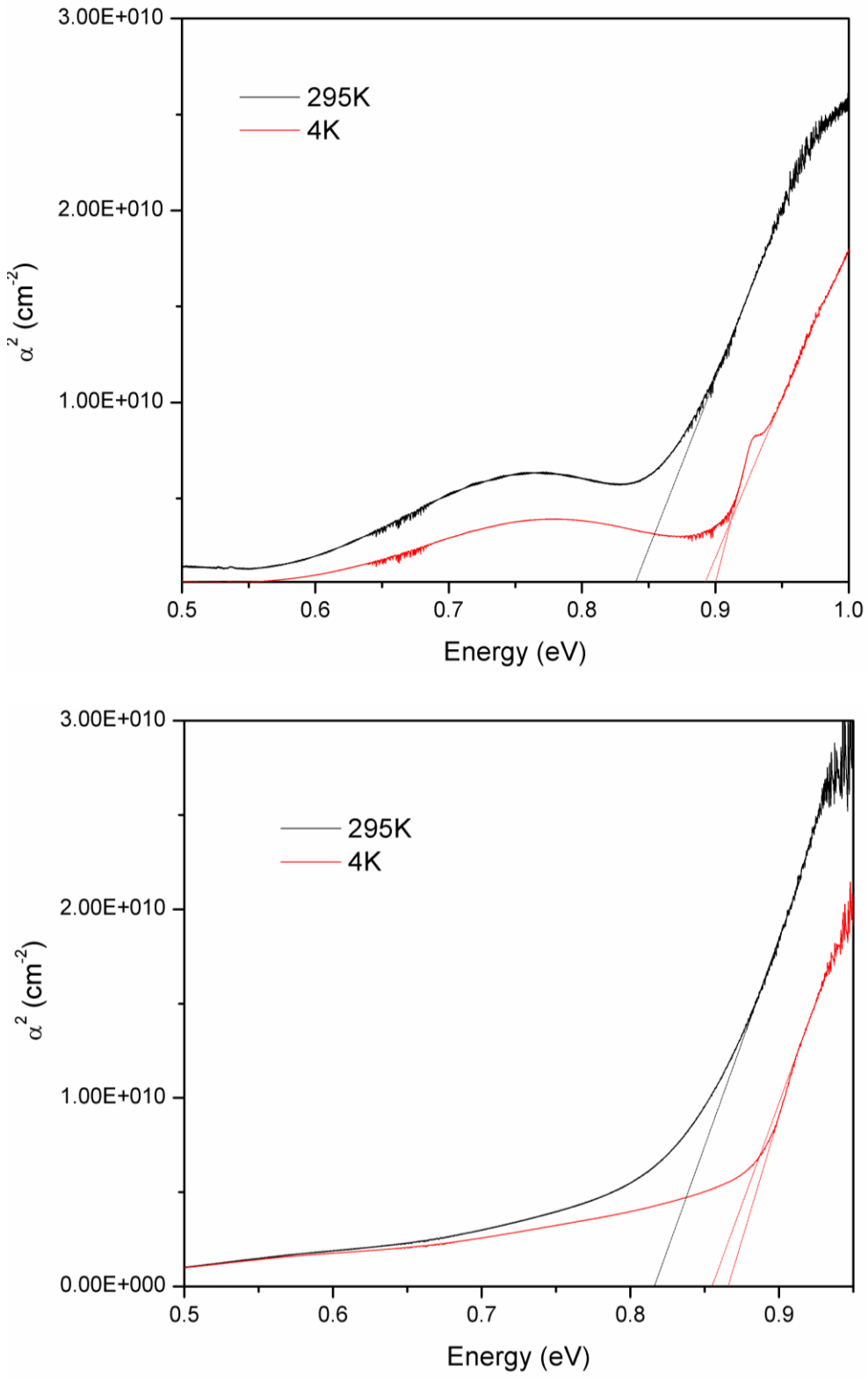

Figure 3.13. FTIR spectra from β-Fe(SiGe)$_2$ with (a) 0.5% Ge and (b) 2.8% Ge

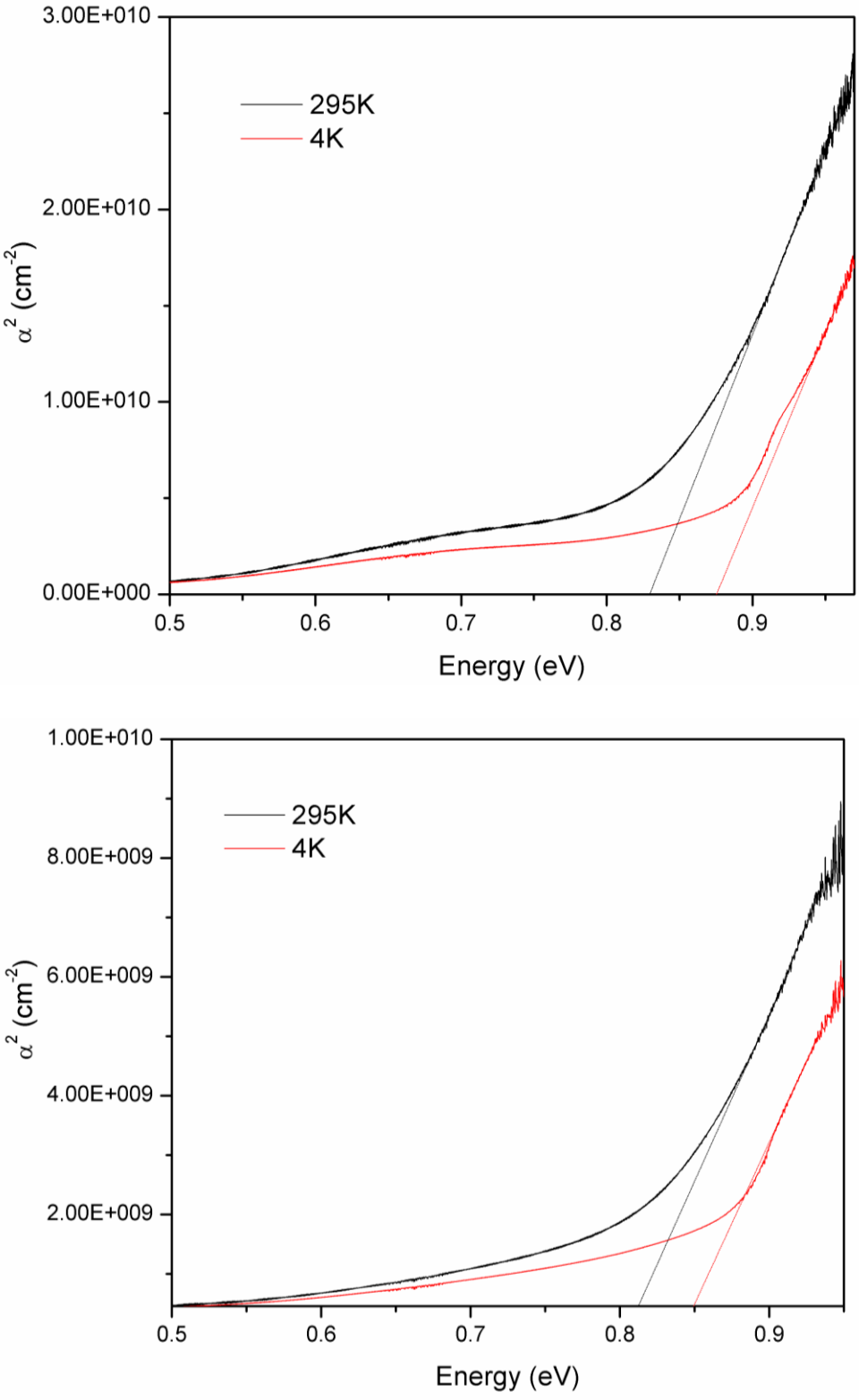

Figure 3.13. FTIR spectra from β-Fe$(SiGe)_2$ with (c) 3.7% Ge (d) nominal 5% Ge with a segregated Ge layer

Absorption spectra for several β-Fe(SiGe)$_2$ samples are presented in Figure 3.13. In general the band gap decreases with increasing Ge content, as predicted Tani and Kido and demonstrated by Chen *et al.*[89,90] The band gaps extracted from each spectrum are plotted in Figure 3.14 as a function of Ge concentration (as measured by RBS). The increase in band gap from the 2.8% Ge sample to the 3.7% Ge sample is likely due to a relaxation in the lattice due to nucleation of Ge crystallites, which is in agreement with the previously demonstrated XRD measurements.

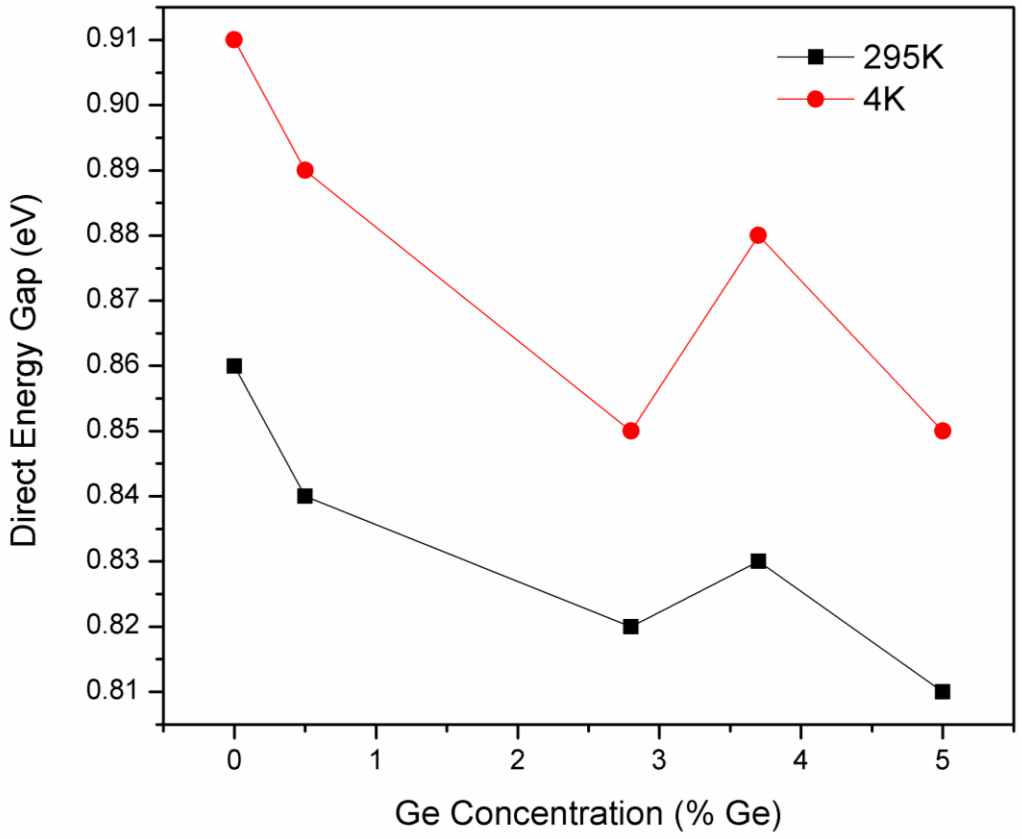

Figure 3.14. Band gap extracted from absorption spectra vs. Ge concentrations of samples as determined by RBS simulations.

Hall Effect Measurements

Electrical transport measurements were conducted between 4 and 300 K for MBE grown β-$FeSi_2$ and β-$Fe(Si_{1-x}Ge_x)_2$ thin films (2000 – 8000Å). Using a 19 kG magnetic field and a current of 20 – 40 μA through indium ohmic contacts, the Hall coefficient was calculated. The results are shown in Figure 3.15 for $0 \leq x \leq 0.15$ nominal Ge concentrations. As has been stated previously, for the x=0.05 and 0.15 samples, RBS and XRD have shown Ge segregation.

Carrier concentrations range from $5x10^{17}$ cm^{-3} (x=0) to $3x10^{19}$ cm^{-3} (x=0.005) at room temperature and $3x10^{17}$ cm^{-3} (x=0) to $1x10^{18}$ cm^{-3} (x=0.005) at 4 K. All samples with $x > 0$ display a sharp rise in mobility starting between 240 and 260 K, whereas the x=0 sample displays a sharp decrease in the carrier concentration and a sharp increase in the mobility at ~130 K. Above 180 K, the mobility of the x=0 sample decreases almost an order of magnitude until, at room temperature, the mobility is 16 $cm^2/V{\cdot}s$. This feature was again seen in our most recent van-der Pauw measurement of this sample. Resistivity was largest in the x=0 sample, ranging from 5.5 to 0.8 Ω·cm at 4 K and RT respectively, and smallest for the x=0.005 sample, ranging from 0.9 to 0.2 Ω·cm at 4 K and RT respectively.

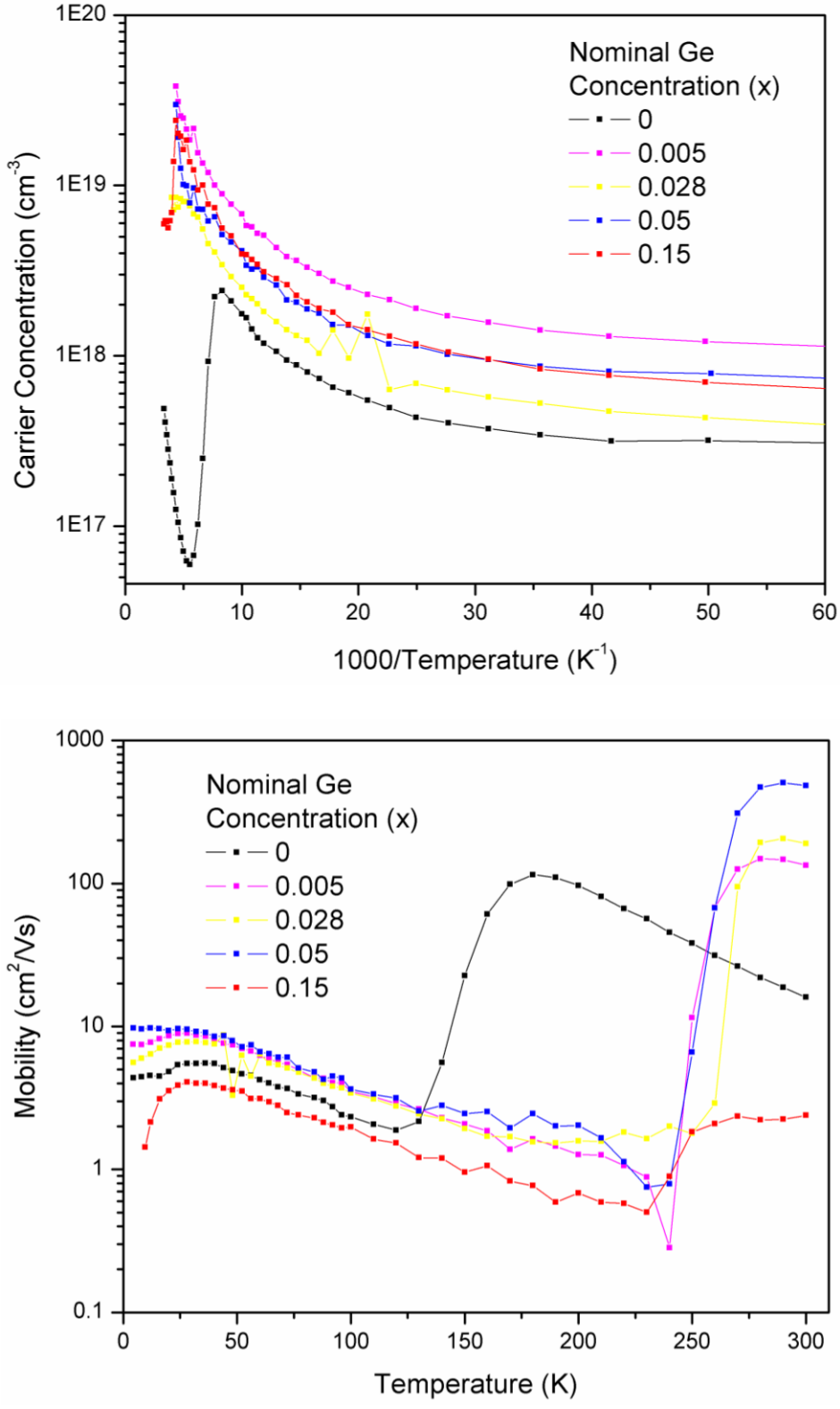

Figure 3.15 (a) Carrier concentration and (b) mobility of β-Fe($Si_{1-x}Ge_x$)$_2$ samples from Hall effect measurements.

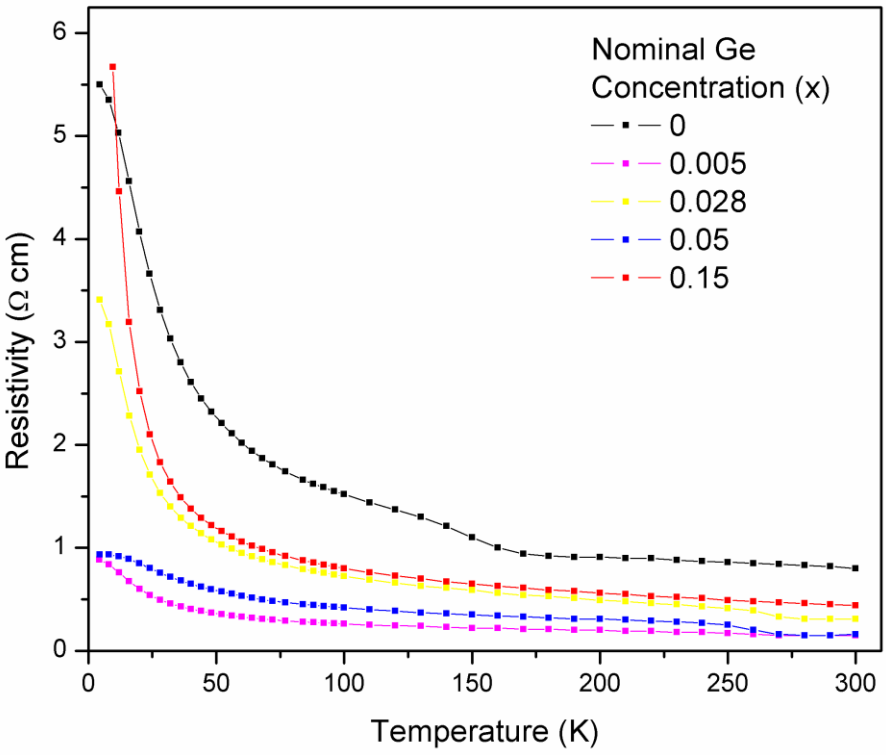

Figure 3.15 (c) Resistivity of β-Fe($Si_{1-x}Ge_x$)$_2$ samples from Hall effect measurements.

CHAPTER 4

OSMIUM SILICIDE GROWTH AND CHARACTERIZATION

Introduction

Osmium monosilicide was reported as early as 1957 using mechanical alloying of compressed and annealed constituent powders.[125] It was determined that the OsSi phase possesses the FeSi cubic crystal structure with space group $P2_13$. Later, Engstrom discovered the $OsSi_2$ phase by arc-melting a mixture of osmium and silicon powders.[126] He concluded $OsSi_2$ is isostructural with β-$FeSi_2$. This was confirmed later by Mason and Muller-Vogt using mechanically alloyed samples as well.[127] A band gap of 1.8 eV was determined using high-temperature resistivity measurements on these samples. It was further determined that an Os_2Si_3 phase occurs which is isostructural to Ru_2Si_3.[128] Thin films of $OsSi_2$ and Os_2Si_3 were formed by deposition of osmium on silicon followed by annealing.[129] It was found that the disilicide phase formed by annealing at 800°C and 1000°C while the Os_2Si_3 phase formed by annealing at 700°C. These films however would peel off the substrate for thicknesses greater than 200 nm.

Schellenberg *et al.* used the mechanical alloying method to establish a phase diagram for Os-Si, the results of which are shown in Figure 4.1.[130] From high temperature resistivity measurements, they determined the band gaps to be ~2.3 eV for Os_2Si_3 and 1.4 eV for $OsSi_2$ as shown in Figure 4.2.

Epitaxial $OsSi_2$ and polycrystalline $OsSi_2$ and Os_2Si_3 were formed on Si(111) using electroless deposition and annealing techniques by Chang and Chou.[131] The

annealing for these samples was two steps of processing at 200°C and 1000°C in a reducing atmosphere consisting of a mixture of hydrogen and argon gas. The orientation observed for the epitaxial films was (040) $OsSi_2$||(220)Si with [102]$OsSi_2$||[111]Si.

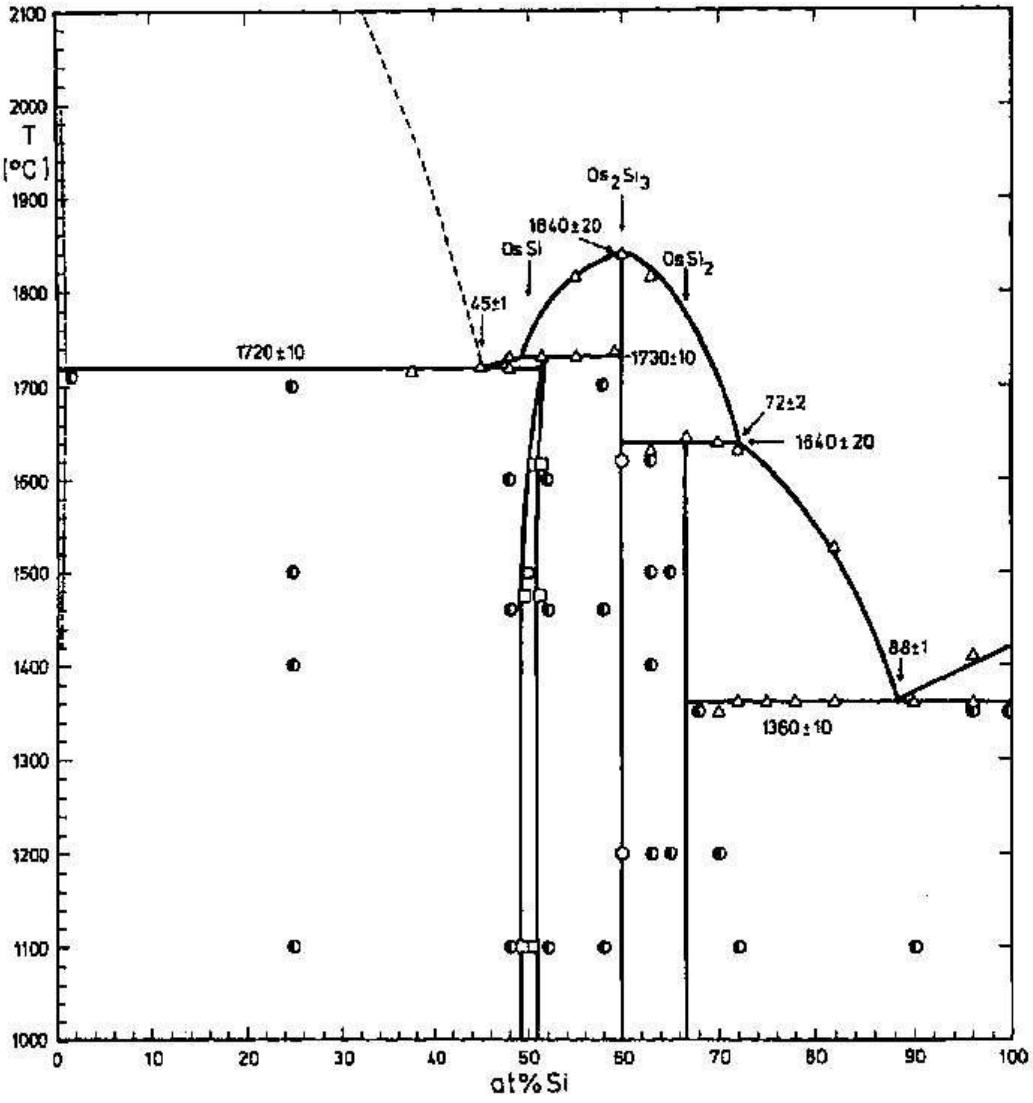

Figure 4.1. The Os-Si phase diagram. [130]

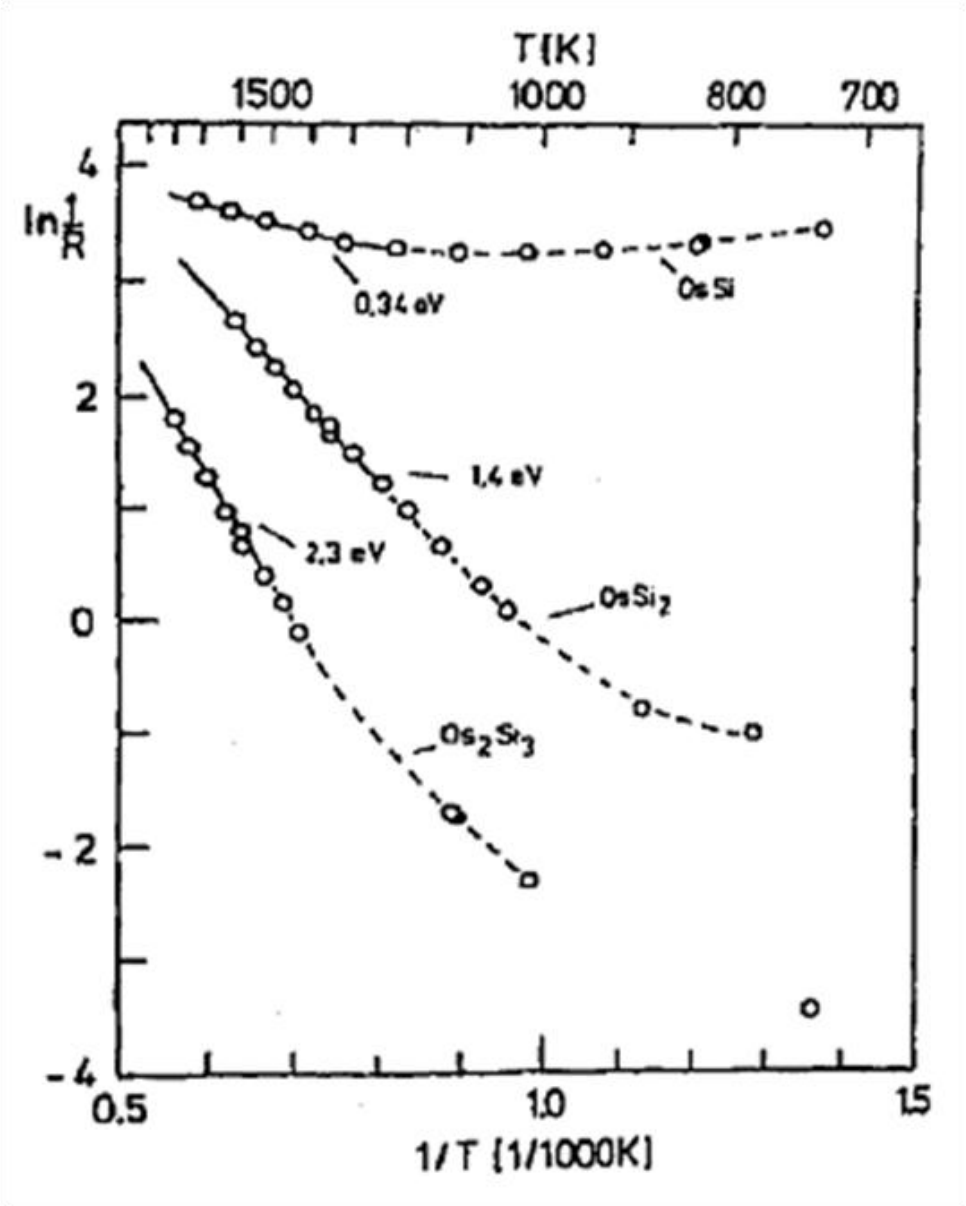

Figure 4.2. High temperature resistivity measurement of the band gap for three phases of osmium silicide. [130]

Recently, Mitchell et al. formed Os_2Si_3 precipitates using ion implantation of osmium into a silicon substrate.[83] These ion beam synthesized samples demonstrated faint visible photoluminescence at ~2.4 eV.

While experimentally the band gap of $OsSi_2$ has been shown to be 1.8 or 1.4 eV by electrical measurements, theoretical reports show $OsSi_2$ to have an indirect band gap

of 0.95 or 0.06 eV.[48,86] Although the band gap of Os_2Si_3 has been estimated from electrical measurements to be 2.3 eV, theoretical reports contradictory to this experimental value have more recently shown Os_2Si_3 to have a direct gap of 0.95 eV.[48]

Of further interest is the theoretical prediction that the ternary $Fe_{0.5}Os_{0.5}Si_2$ possesses a direct gap of 0.76 eV.[132] This encourages the possibility that an alloy between isostructural β-$FeSi_2$ and $OsSi_2$ may provide a ternary system for band-gap engineering. Isostructural Ru_2Si_3, Ru_2Ge_3, Os_2Si_3, and Os_2Ge_3 may also provide a basis for band-gap engineering. However, there has been very little work on this system

This is a report of MBE growth of osmium silicides with emphasis on phase identification. Growth parameters, RHEED images and intensity oscillations, and preliminary x-ray diffraction are included.

Thin Film Growth

Osmium silicide thin films (146-410 Å) were prepared on 2 in. Si (100) wafers in a UHV Instruments MBE system described in Chapter 2. The Si substrates were cleaned by the Shiraki method,[133] and, following the final oxide formation, the substrates were introduced into a deposition chamber (base pressure of 4×10^{-11} Torr) and heated to 800ºC for 45 min to remove the oxide layer. A 50 nm Si buffer layer was then grown at 550ºC at ~1 Å/s followed by Os and Si co-deposition.

A one inch disc of compressed Os powder, 3N pure, was *e*-beam evaporated in a W crucible. Due to the strikingly low vapor pressure of Os (2.52 Pa at 3300 K compared to 4.77 Pa at 1683 K for Si), the growth rate was dominated by an Os flux of

10^{13}–10^{14} atoms/cm^{2}s. This flux was calibrated by Rutherford backscattering spectroscopy and stabilized during growth within +/-5%. The Si flux was *e*-beam evaporated from a 43cc single crystal FZ ingot and calibrated by RHEED intensity oscillations. Sample #1 (single phase) was grown with a substrate temperature of 700ºC, Os flux of 1.38 x 10^{14} atoms/cm^{2}s, a Si/Os flux ratio of 4.2, and a total thickness of 410 Å. For sample #2 (multi-phase), a substrate temperature of 625ºC, Os flux of 2.65 x 10^{13} atoms/cm^{2}s, and a flux ratio of 1.5 were used resulting in a total thickness of 146 Å. The two samples chosen for this study are representative of the crystalline phase obtained for each flux ratio, although similar samples have been prepared with temperatures ranging from 600-700ºC. The flux ratio greatly affected the resulting phase of our films.

A Staib Instruments, Model 15-S, RHEED gun was used *in situ* to determine epitaxial growth, and RHEED intensity oscillations were observed for both samples. This was used to determine phase and thickness of our films.

Streaked RHEED patterns were observed during growth, as seen in Figure 4.3. The Os_2Si_3 patterns shown were taken at 0º, 45º, and 90º away from the Si [110] azimuth. RHEED intensity oscillations are shown in Figure 2 and suggest a growth rate of 1.7 ML/s and showed a growth rate of 0.62 Å/s, in agreement with calibration performed by RBS. For growth at a stoichiometric flux ratio, J_{Si} /J_{Os}=1.5, multiphase films tended to form. For a more silicon-rich flux ratio, J_{Si} /J_{Os}=~4, single phase Os_2Si_3 films are observed.

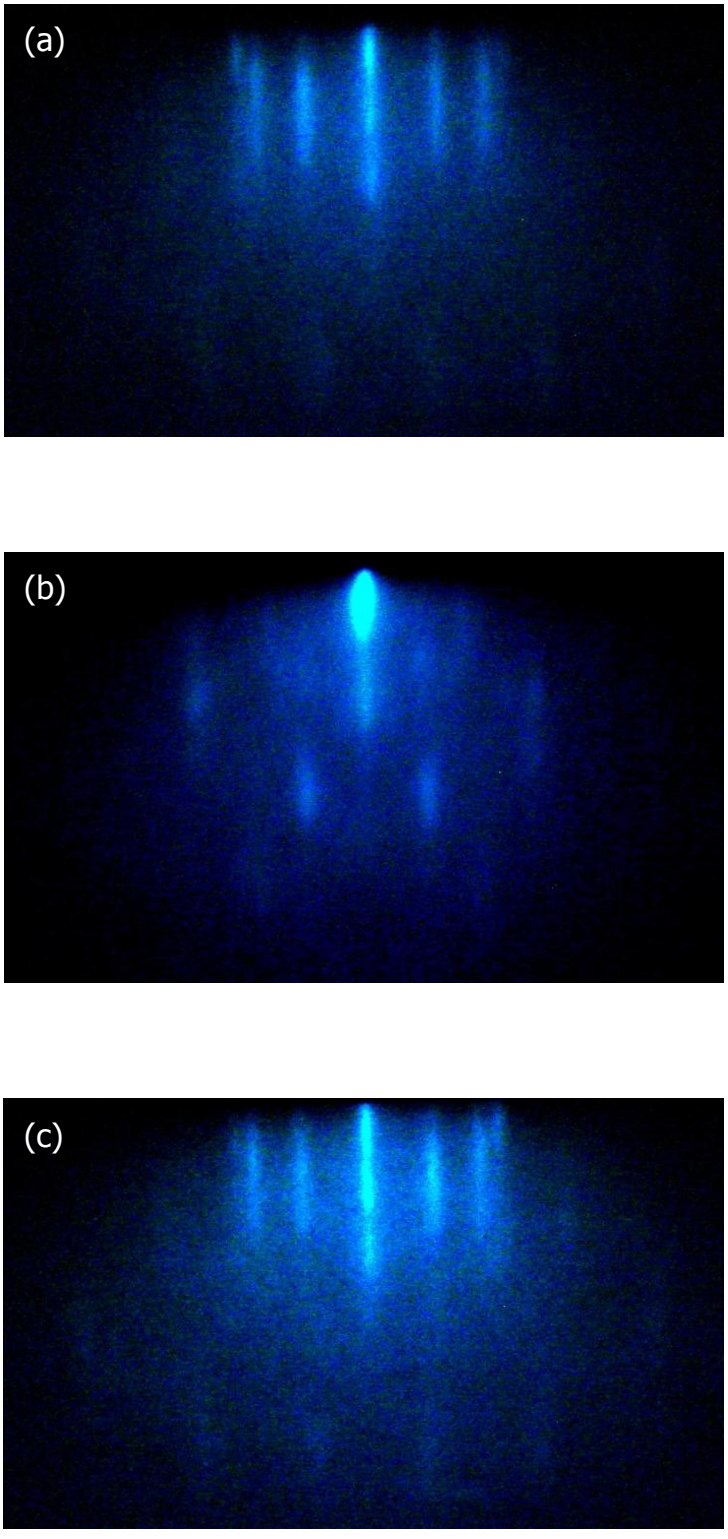

Figure 4.3. Streaked RHEED pattern from single crystalline Os_2Si_3. Pictures taken (a) 0º, (b) 45º, and (c) 90º from Si [110] azimuth.

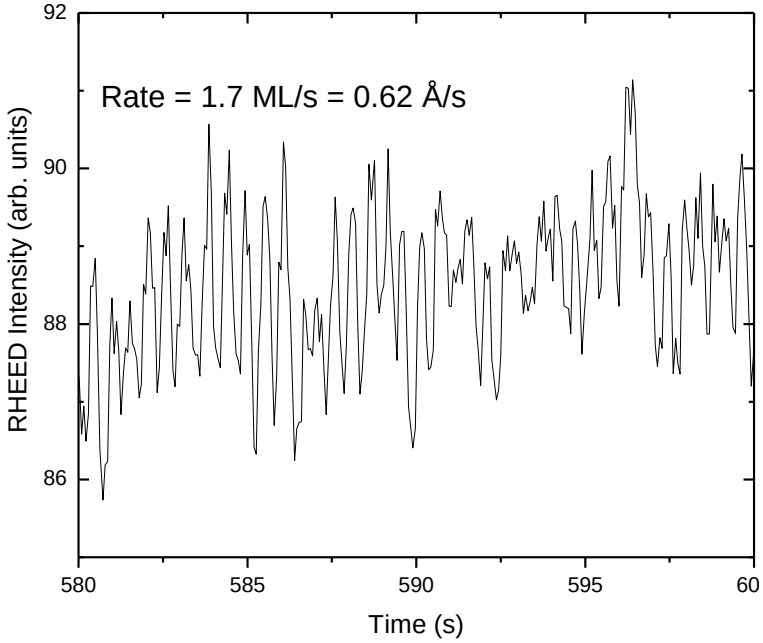

Figure 4.4. RHEED intensity oscillations collected during osmium silicide film growth, showing a growth rate of 0.62 Å/s

X-Ray Diffraction

XRD measurements were performed using a four-circle Huber diffractometer mounted at a rotating anode with a copper target and a maximum power of 12 kW. A flat Ge(2 2 0) monochromator at wavelength 1.5406 Å was used for out-of-plane data analysis in the [0 0 1] direction of the Si substrate. The scans were taken at 40 kV with a current of 130 mA. The in-plane data were obtained using a 100mm precession camera with a sealed silver X-ray tube and a graphite monochromator; the precession camera is an instrument to produce undistorted images of a plane in reciprocal space. The data were collected on an image plate and read out using a 12-bit analog-digital converter with a lateral resolution of 0.1 mm. The power used was 25mA and 40 kV, with a screen radius of 10 mm, a screen–sample distance of 27.5 mm, and an opening

angle of 20°. The data were taken in the {h k} plane keeping the l direction constant at zero.

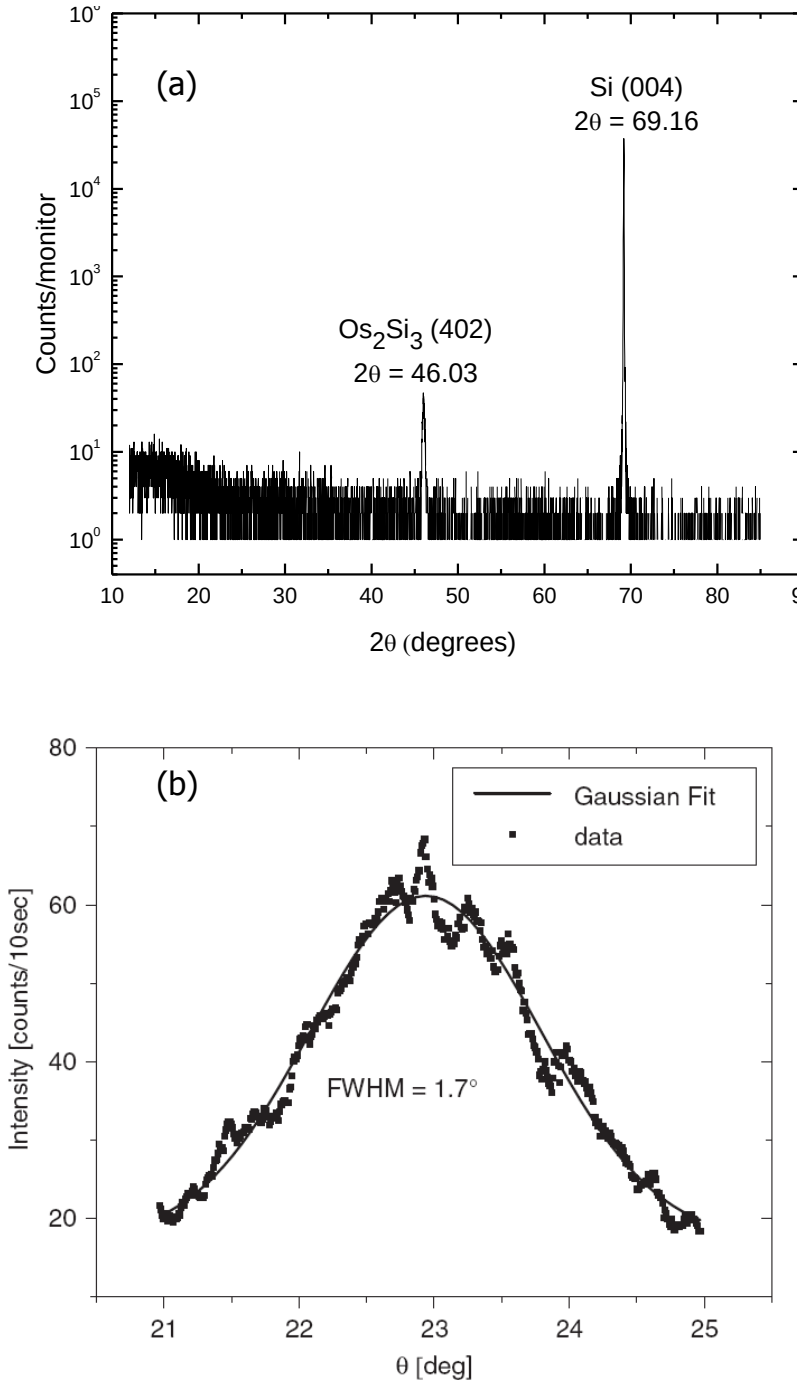

Figure 4.5. X-ray diffraction spectra of (a) single crystalline Os_2Si_3 demonstrating an epitaxial orientation of Os_2Si_3(402)/Si(100), (b) rocking curve of showing a width of 1.71.

Figure 4.5a shows a θ–2θ scan in the direction of the surface normal. Two peaks, the Si (0 0 4) peak at 69.1591 and a single film peak at 2θ=46.0281, are visible. From the rocking curve of the film peak, shown in Fig. 4.5b, the mosaicity of about 1.71 was determined from a full width half-maximum (FWHM) of a Gaussian fit to the data. The oscillations in the rocking-curve data indicate the presence of individual crystallites in the film; the film is therefore composed of several large crystallites with some small angle grain boundaries in between. X-ray reflectivity measurements have been performed in order to determine the morphology of these crystallites. The data are shown in Figure 4.6 together with a fit to the data using a simple dynamical scattering model shown in the inset. The fitting parameters were the thickness of the film, the surface and interface roughness and the electron density parameter 2δ, which is the real part of the refractive index. The thickness of the film as determined by fitting was 350Å, which correlated well with the nominal growth thickness of 400Å. The surface and the interfacial roughness were determined to be 30 and 18Å, respectively.

The single film peak observed in Figure 4.5a indicates the growth of single-phased osmium silicide; however, it is not clear if this is a phase of OsSi, $OsSi_2$ or Os_2Si_3. The angle of this peak could correspond to OsSi (2θ=47.06251), $OsSi_2$ (2θ=46.075) or Os_2Si_3 (2θ=46.124) based on the calculations given by Petersson *et al.*[134] To unambiguously determine the phase of this sample, in-plane measurements using a precession camera in transmission mode were taken in the {hk0} plane, with the l direction fixed and perpendicular to the sample. The results are shown in Figure

4.7, where the large black spots represent the silicon reflections, and the small black spots are the Os_xSi_y reflections.

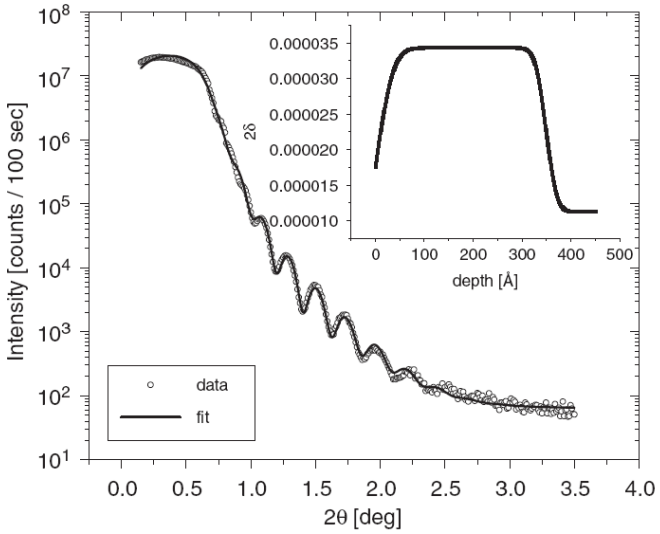

Figure 4.6. X-ray reflectivity measurements of the single phased osmium silicide film. The inset shows the model underlying the fit.

The gray scale is a representation of the scattered intensity on a logarithmic scale. Fits to the in-plane data was performed using crystallographic simulation software. The best fit to the experimental data was obtained with Os_2Si_3 (4 0 2) plane parallel to the Si(0 0 1). As shown in Fig. 4.7, two Os_2Si_3 domains rotated by 90°, indicated by the two rectangles, are present. This is plausible assuming that the fourfold substrate symmetry gives rise to two equally populated twofold crystallographic domains. The reflections contained in each domain are indexed as (-2 2 4), (-2 -2 4), (2 -2 -4), and (2 2 -4). Taking into account the finite resolution of the precession photograph (1.2% of the lattice parameter, largely given by the pixel resolution), the lattice parameters calculated coincide with the bulk values and are a= 11.12, b= 8.902 and c=5.57 Å.[55] These experimental parameters have been used to model the Os_2Si_3 structure shown in Figure 4.8.

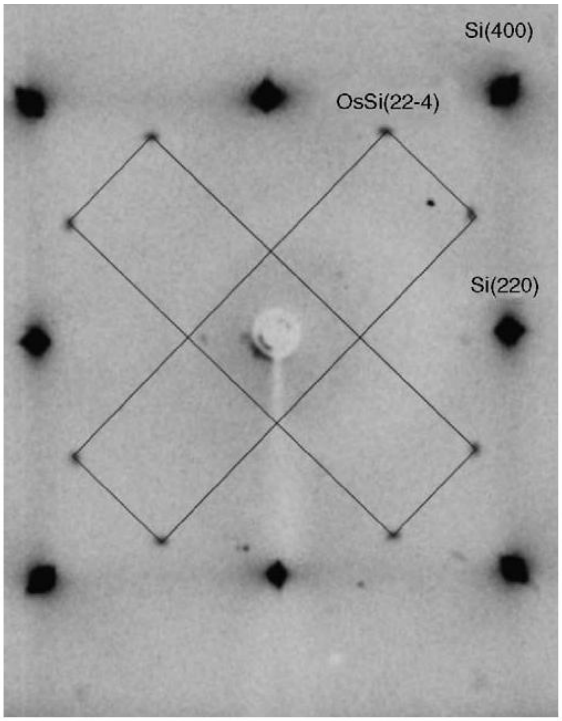

Figure 4.7. In-plane data in the (h k 0) plane from the precession camera. The two rectangles indicate the orientation of two crystallographic domains perpendicular to each other

The XRD θ-2θ scan for sample #2, shown in Figure 4.9, has three peaks corresponding to the thin film. The peak at 2θ = 47.71° represents either $OsSi_2$ (422) or (204) plane. These two cannot be delineated simply by out-of-plane XRD since their d-spacings are similar. The other two peaks are very weak and can be seen just to the left of the Si(002) peak. The 2θ = 32.34° peak results from either the (200) or the (004) plane of Os_2Si_3. Finally, the peak at 2θ = 31.76° has not been identified as any osmium silicide phase. Therefore, for this sample there are at least two separate phases of osmium silicide with the Os_2Si_3 phase oriented differently than the single phase sample.

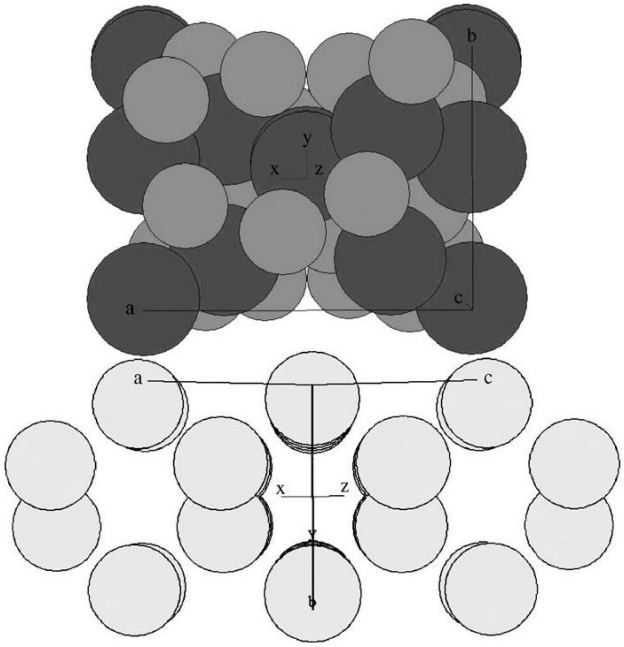

Figure 4.8. Real-space model based on the experimentally determined lattice parameters. Only one crystallographic domain is shown. Large circles represent Os atoms; small circles are Si atoms.

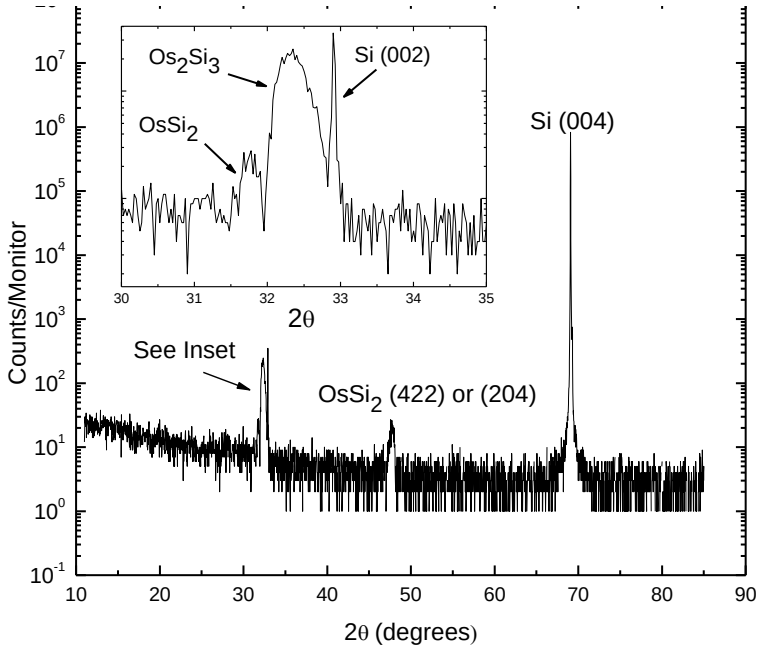

Figure 4.9. X-ray diffraction spectra of multiphase osmium silicide with inset showing detail around the Si(002) peak.

Scanning Electron Microscopy

A FEI Nova Nanolab 200 Dual Beam FEGSEM was used to conduct scanning electron microscopy for qualitative observation of film roughness and phase separation. Field emission SEM images of samples #1 and #2 at 150,000X using a 15kV beam are shown in Figure 4.10 (a) and (b) respectively. Sample #1 is significantly more uniform in roughness compared to sample #2. Further, sample #2 appears to be segregated into at least three phase/orientations as indicated by the arrows in the image.

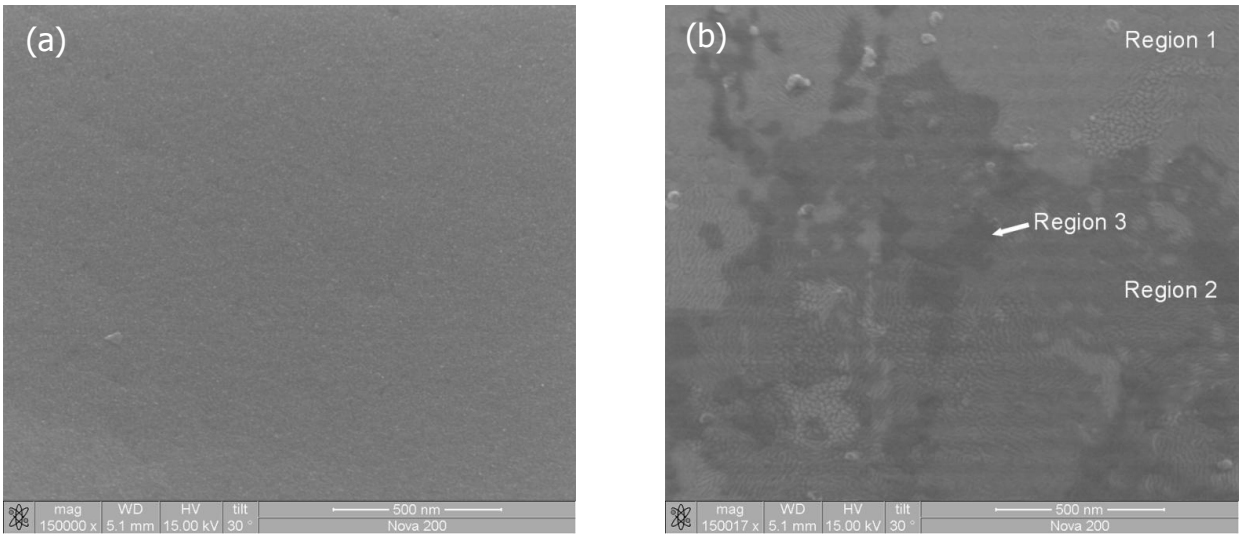

Figure 4.10. Scanning electron micrograph of (a) single crystalline Os_2Si_3 (Sample 1) and (b) polycrystalline $OsSi_2$ and Os_2Si_3 (Sample 2). Sample 2 shows at least three significant regions, each corresponding to some phase or orientation of osmium silicide.

Absorption

Transmission spectrum for the sample was taken using a Bruker high-resolution Fourier transform infrared spectrometer (FTIR) in transmission mode. The sample was mounted on cold finger and installed in a LN2-cooled Janis cryostat. Data was taken

under vacuum at room temperature and at 77 K. Absorption spectra were taken in the NIR region (0.15- 1.24 eV) with a Tungsten source and signal collected with a cooled InSb detector. Substrate-related absorption effects were subtracted from the data using a bare Si substrate as the background. The data was smoothed by 25-point adjacent averaging.

The absorption coefficient extracted from the transmission data at RT 77K is shown in Figure 4.11. The intercept of a linear fit to the data yields a direct band gap of 1.01 eV at 77 K, which is in reasonable agreement with the results calculated by the LMTO method reported by Filonov *et al.*[48]

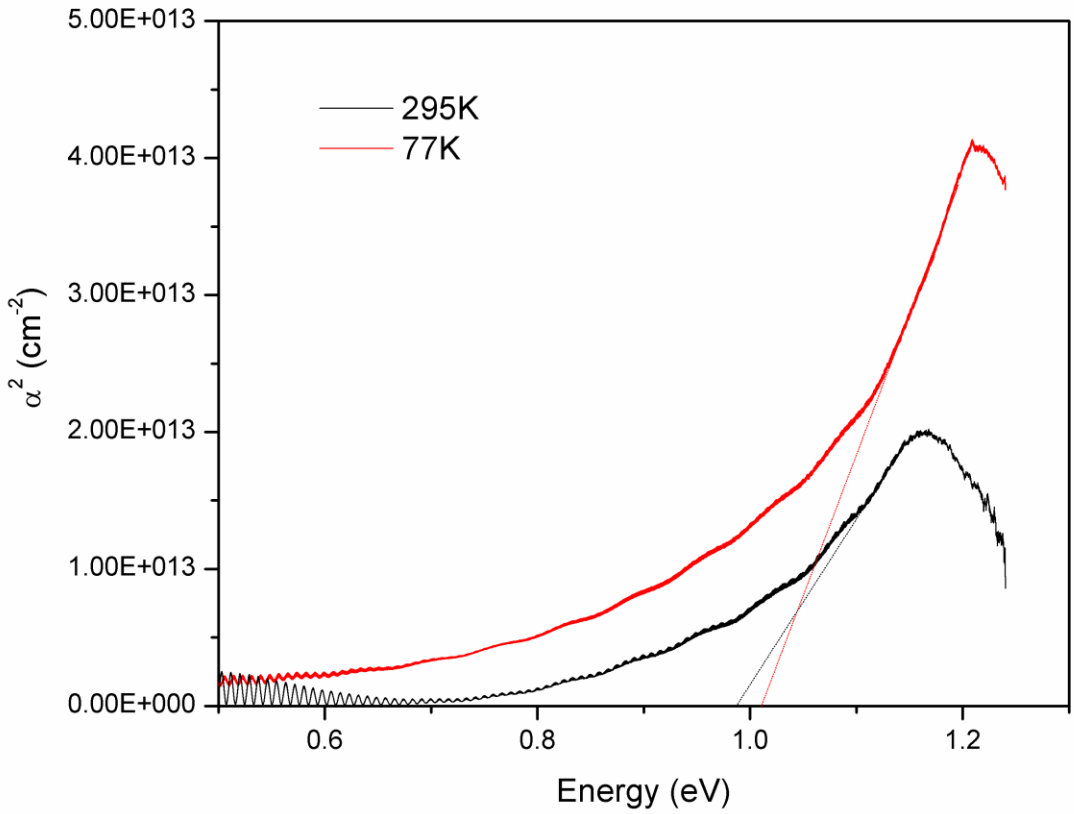

Figure 4.11. Absorption spectra of single phase Os_2Si_3 at RT and 77K.

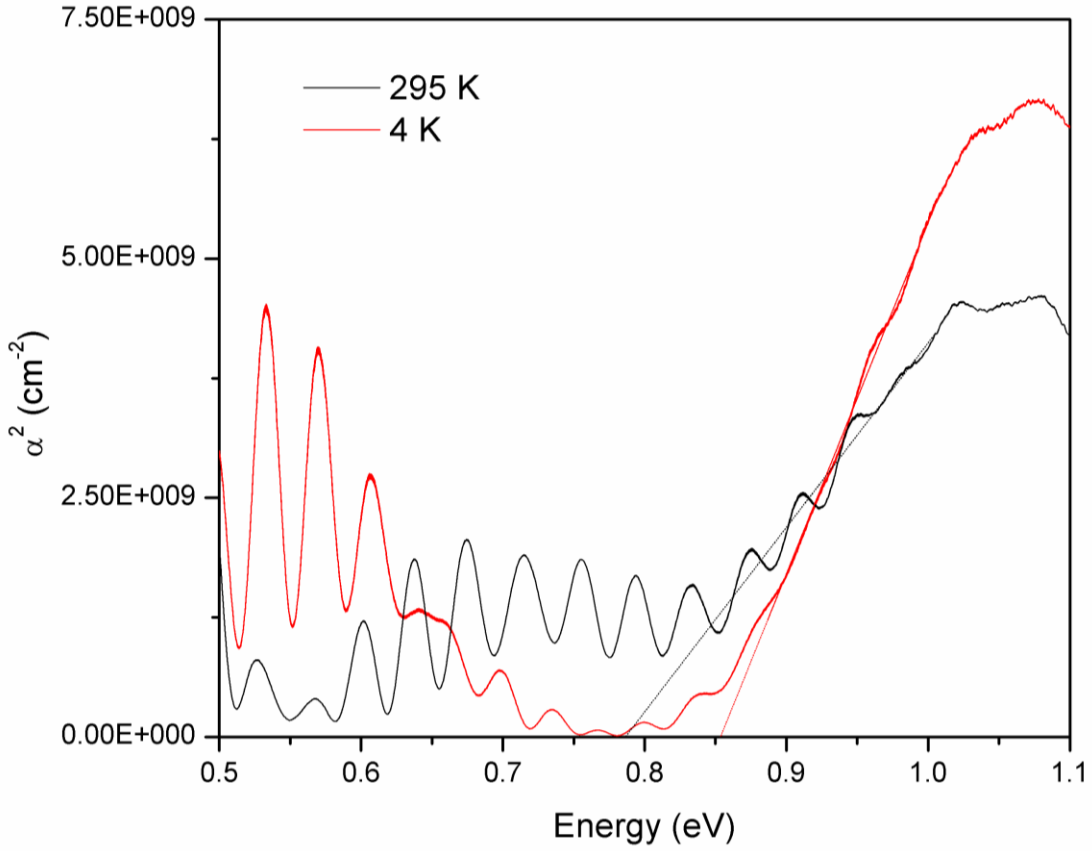

Figure 4.12. Absorption spectra for multiphase osmium silicide sample at RT and 77K.

The absorption coefficient extracted from the transmission data at 77K is shown in Figure 4.11. The complex mixture of phases along with the thinness of the film (146 Å compared to 410 Å for the single phase sample) makes it difficult to extract much information from this data. However some absorption edge can be distinguished around 0.78 eV at RT and 0.85 eV at 77 K. This is significantly lower than the band gaps of the identified phases (Os_2Si_3 and $OsSi_2$).

Magneto-Transport

Temperature dependent Hall effect measurements were performed from 77 K to room temperature on a range of samples including three single phase films and three multiphase films. The magnetic field was 10 kG and the current was 0.1 μA. The results are shown in Figure 4.13 and labeled according to the substrate temperature during growth.

The room temperature (RT) carrier concentration for most samples was on the order of $1x10^{19}$ cm^{-3}. One multiphase sample showed a larger carrier concentration on the order of $1x10^{20}$. Most samples (multiphase and single phase) demonstrate electrical properties which are well behaved in the intrinsic conduction region but show an increase in mobility of one to three orders of magnitude starting between 80 and 100 K due to the onset of multiple charge carriers. However, one single phase sample (▪) decreases over the entire temperature range from 6000 to 80 $cm^2/V{\cdot}s$ at 4 K and RT respectively. From this data, it appears that the electrical properties of these samples cannot be predicted based on the phases identified. This is likely due to variations in crystalline quality as well as the dissimilar relative concentrations of phases within the multiphase samples.

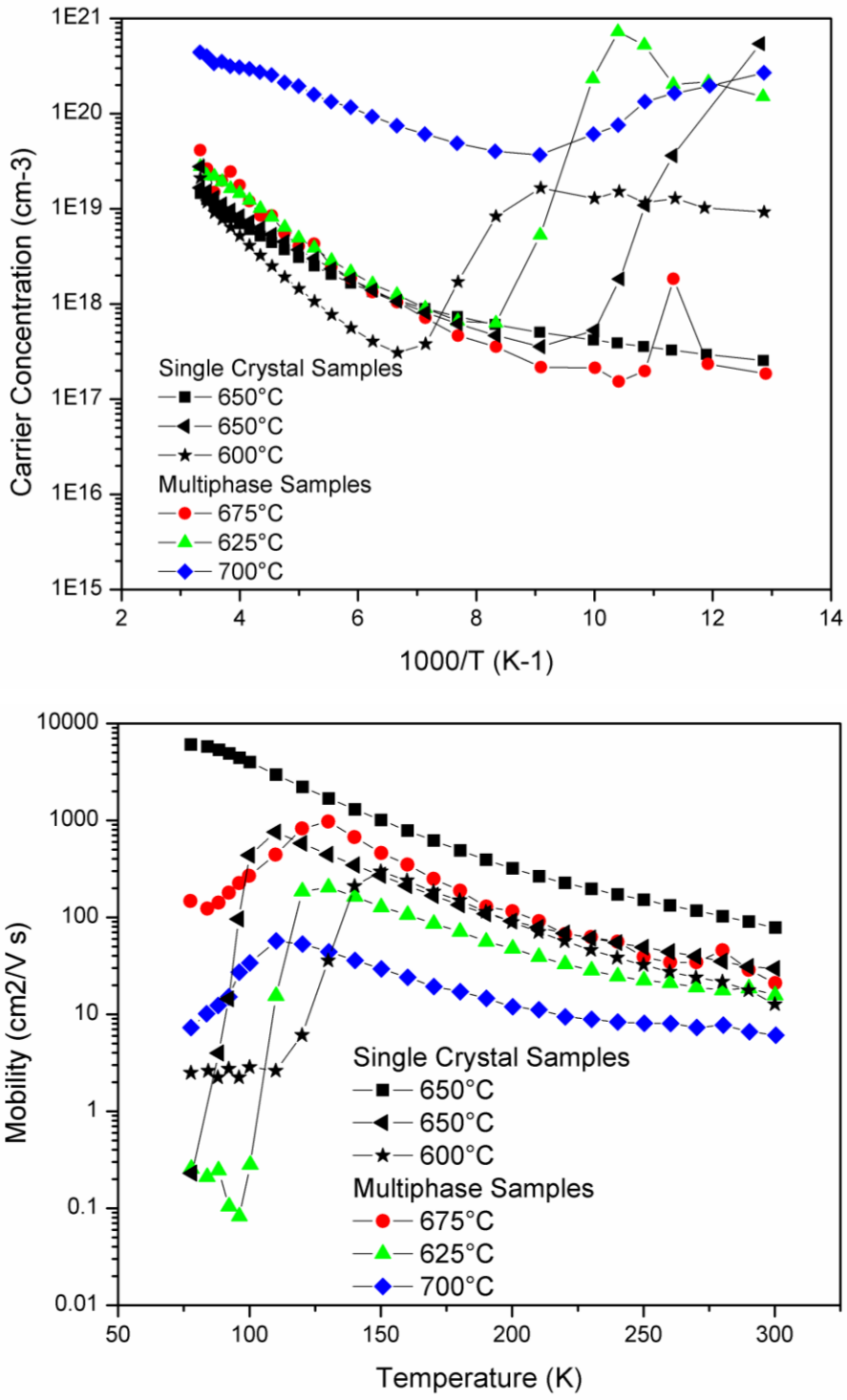

Figure 4.13. Temperature Hall effect measurements yielded the (a) carrier concentration and (b) mobility of single phase Os_2Si_3 and multiphase Os-Si films. The legend shows the growth temperature for each sample.

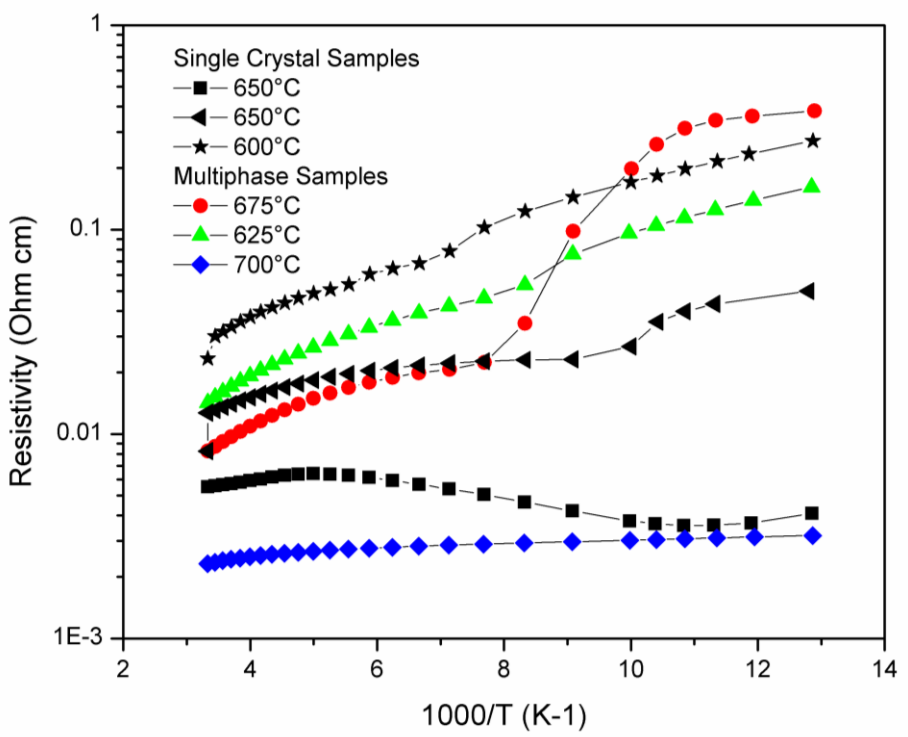

Figure 4.13. Temperature Hall effect measurements yielded the (c) resistivity of single phase Os_2Si_3 and multiphase Os-Si films. The legend shows the growth temperature for each sample.

CHAPTER 5

CONCLUSIONS

There would be considerable benefits from the development of a ternary semiconducting silicide-based material system with a tunable band gap. For instance, a variety of optoelectronic devices could be developed from β-$Fe(SiGe)_2$ if it can be proven a feasible alloy with broad enough control over the bandgap energy. The addition of Ge to the β-$FeSi_2$ lattice will only be possible to the point that it becomes energetically favorable for the Ge to segregate into some FeGe or SiGe phase or as Ge crystallites. This creates immediate questions about the alloy range that can be achieved through nonequilibrium growth techniques such as molecular beam epitaxy (MBE).

β-$Fe(Si_{1-x}Ge_x)_2$ ($0 \leq x \leq 0.15$) films have been grown by MBE. The author has performed compositional and structural characterization by XRD and RBS and presented a set of thin films with varying Ge content. These films displayed band gaps ranging from 0.81 to 0.86 eV at room temperature and 0.85 to 0.91 eV at 4 K. A band gap reduction as a function of increasing Ge concentration was observed which is in good agreement with theoretical predictions. However, Ge segregation has been observed in the silicide layers, and have not been able to realize high quality crystalline epilayers for Ge concentrations greater than 4%. This composition value is of interest since similar "upper limit" values for Ge content have also been observed using both reactive deposition epitaxy and solid-phase growth. Clearly, any promise of the use of β-$Fe(Si_{1-x}Ge_x)_2$/$Fe(Si_{1-y}Ge_y)_2$ heterojunctions and multilayers for electro-optical devices

demands that the materials can be synthesized across a greater alloy composition range. Further growth studies of this system are therefore required to establish whether the alloy range in β-Fe($Si_{1-x}Ge_x$)$_2$ epilayers can be successfully increased.

Osmium silicide thin films have been grown by MBE. The author has found that the phase obtained is highly dependent on the Si/Os flux ratio. For a stoichiometric ratio (Si/Os = 1.5) epitaxial, multi-phase films tend to form. If this ratio is raised to ~4, epitaxial, single-phase films occur.

X-ray measurements have been performed on a single phase osmium silicide thin film grown on a Si(1 0 0). The out-of-plane data show that the film grows along its [4 0 2] direction, with a good crystal quality as evidenced by the small FWHM in the rocking curve. The in-plane data show growth twins with perpendicular orientation to each other. The combined in-plane and out-of-plane data indicate that the sample is a single-phase, Os_2Si_3. Absorption analysis yields a band gap comparable to that obtained theoretically. The results show the possibility of growing an epitaxial single-phase Os_2Si_3 thin film by MBE where the growth parameters are crucial in obtaining single-phased films.

The author believes the investigation of semiconducting silicides should continue with particular focus on the multifunctional characteristics of many of the materials including β-$FeSi_2$ which demonstrates thermoelectric and ferromagnetic characteristics. Germanide counterparts for Os_2Si_3 and Ru_2Si_3 may still provide ternary systems for band gap engineering. Further, very little growth transition metal-side ternaries have

been attempted. Although this study has shown limited bandgap tunability of the Fe-Si-Ge ternary, the semiconducting silicides remain a promising set of versatile materials.

BIBLIOGRAPHY

[1] D. J. Lockwood, R. K. Willardson, and E. R. Weber, *Light Emission in Si: From Physics to Devices* pp. 6-26 (Academic Press, New York, 1997).

[2] Q. Mi, X. Xiao, J. C. Sturm, L. C. Lenchyshyn , and M. L. W. Thewalt, Appl. Phys. Lett. **60**, 3177 (1992).

[3] H. Presting, T. Zinke, A. Splett, H. Kibbel, and M. Jaros, Appl. Phys. Lett. **69**, 2376 (1996).

[4] H. Ennen, G. Pomrenke, A. Axmann, K. Eisele, W. Haydl, and J. Schneider, Appl. Phys. Lett. **46**, 382 (1985).

[5] L. T. Canham, K. G. Barraclough, and D. J. Robbins, Appl. Phys. Lett. **51**, 1509 (1987).

[6] P. L. Bradfield, T. G. Brown, and D. G. Hall, Appl. Phys. Lett. **55**, 100 (1989).

[7] J. Michel, J. L. Benton, R. F. Ferrante, D. C. Jacobson, D. J. Eaglesham, E. A. Fitzgerald, Y. –H. Xie, J. M. Poate, and L. C. Kimerling, J. Appl. Phys. **70**, 2672-8 (1991).

[8] J. Palm, F. Gan, B. Zheng, J. Michel, and L. C. Kimerling, Phys. Rev. B **54**, 17603 (1996).

[9] A. D. Yoffe, Adv. Phys. **42**, 173 (1993).

[10] L. Brus, Appl. Phys. A **53**, 465 (1991).

[11] U. Gnutzmann and K. Clausecker, Appl. Phys. **3**, 9 (1974).

[12] B. Hollander, S. Mantl, B. Stritzker, F. Schaffler, H. J. Herzog, and E. Kasper, Appl.

Surf. Sci. **50**, 450 (1991).

[13] T. P. Pearsall, Prog. Quant. Electron. **18**, 97 (1994).

[14] U. Schmid, J. Humlicek, F. Lukes, M. Cardona, H. Presting, H. Kibbel, E. Kasper, K. Eberl, W. Wegscheider, and G. Abstreiter, Phys. Rev. B **45**,6793 (1992).

[15] L. T. Canham, Appl. Phys. Lett. **57**, 1046 (1990).

[16] A. G. Cullis and L. T. Canham, Nature **353**, 335 (1991).

[17] V. Lehmann and U. Gosele, Appl. Phys. Lett. **58**, 856 (1991).

[18] A. Bsiesy, J. C. Vial, F. Gaspard, R. Herino, M. Ligeon, F. Muller, R. Romestain, A. Wasiela, A. Halimaoui, and G. Bomchil, Surf. Sci. **254**, 195 (1991).

[19] N. Koshida and H Koyama, Jpn. J. Appl. Phys. 1 **30**, L1221 (1991).

[20] Z. Lu, D. J. Lockwood, and J. –M Baribeau, Nature **378**, 258 (1995).

[21] J. Lee, S. H. Li, J. Singh, and P. K. Bhattacharya, J. Electron. Mater. **23**, 831 (1994).

[22] Y. S. Tang, C. D. W. Wilkinson, C. M. Sotomayor Torres, D. W. Smith, T. E. Whall, and E. H. C. Parker, Appl. Phys. Lett. **63**, 497 (1993).

[23] N. Usami, T. Mine, S. Fukatsu, and Y. Shiraki, Appl. Phys. Lett. **63**, 2789 (1993).

[24] Y. S. Tang, C. M. Sotomayor Torres, B. Dietrich, W. Kissinger, T. E. Whall, and E. H. C. Parker, J. Cryst. Growth **157**, 280 (1995).

[25] R. Apetz, L. Vescan, A. Hartmann, C. Dieker, and H. Luth, Appl. Phys. Lett. **66**, 445 (1995).

[26] Y. Kanemitsu, K. Suzuki, M. Kondo, S. Kyushin, and H. Matsumoto, Phys. Rev. B **51**, 10666 (1995).

[27] M. Stutzmann, M. S. Brandt, M. Rosenbauer, J. Weber, and H. D. Fuchs, Phys Rev. B **47**, 4806 (1993).

[28] Deak, P., Rosenbauer, M., Stutzmann, M., Weber, J., and Brandt, M. S., Phys. Rev. Lett. **69**, 2531 (1992).

[29] Stutzmann, M., Brandt, M. S., Rosenbauer, M., Fuchs, H. D., Finkbeiner, S., Weber, J., and Deak, P., J. Lumin. **57**, 321 (1993).

[30] M. A. Lourenco, R. M. Gwilliam, G. Shao, and K. P. Homewood, Mat. Res. Soc. Symp. Proc. **719**, 115 (2002).

[31] S. S. Iyer and Y. –H. Xie, Science **260**, 40 (1993).

[32] R. Soref, Superlattice. Microst. **14**, 189 (1993).

[33] M. Sugo, H. Mori, Y. Sakai, and Y. Itoh, Appl. Phys. Lett. **60**, 472 (1992).

[34] V. E. Borisenko and A. B. Filonov, *Semiconducting Silicides*, edited by V. E. Borisenko (Springer-Verlag, Berlin 2000).

[35] M. Milosavljevic, G. Shao, R. M. Gwilliam, C. Jeynes, C. N. McKinty, and K. P. Homewood, Nucl. Instrum. Meth. B **175-177**, 309 (2001).

[36] D. Leong, M. Harry, K. J. Reeson, and K. P. Homewood, Nature **387**, 686 (1997).

[37] L. Miglio, V. Meregalli, and O. Jepsen, Appl. Phys. Lett. **75**, 385 (1999).

[38] C. Spinella, S. Coffa, C. Bongiorno, S. Pannitteri, and M. G. Grimaldi, Appl. Phys. Lett. **76**, 173 (2000).

[39] S. J. Clark, H. M. Al-Allak, S. Brand, and R. A. Abram, Phys. Rev. B **58**, 10389 (1998).

[40] Z. Yang, K. P. Homewood, M. S. Finney, M. A. Harry, and K. J. Reeson, J. Appl. Phys

78, 1958 (1995).

[41] D. B. Migas, W. Henrion, M. Rebien, V. L. Shaposhnikov, V. E. Borisenko, and L. Miglio, Opt. Mater. **17**, 335 (2001).

[42] J. van Ek, P. E. A. Turchi, and P. A. Sterne, Phys. Rev. B **54**, 7897 (1996).

[43] G.V. Samsonov, I.M. Vinitskii: *Handbook of Refractory Compounds*, (IFI/Plenum, New York, 1980).

[44] H. Lange, W. Henrion, B. Selle, G. -U. Reinsperger, G. Oertel, and H. von Kanel, Appl Surf. Sci. **102**, 169(1996).

[45] S. Eisebitt, J. -E Rubensson, M. Nicodemus, T. Boske, S. Blugel, W. Eberhardt, K. Radermacher, S. Mantl, and G. Bihlmayer, Phys. Rev. B **50**, 18330 (1994).

[46] K. Maex, M. Van Rossum, and A. Reader, in *Properties of Metal Silicides*, edited by K. Maex, M. Van Rossum (INSPEC, IEE, London, 1995), p. 3-14.

[47] J. Evers and A. Weiss, Mater. Res. Bull. **9**, 549 (1974).

[48] A. B. Filonov, D. B. Migas, V. L. Shaposhnikov, N. N. Dorozhkin, V. E. Borisenko, and H. Lange, Appl. Phys. Letters **70**, 976 (1997).

[49] S. H. Halilov and E. T. Kulatov, Semicond. Sci. Technol. **7**, 368 (1992).

[50] M. C. Bost and J. E. Mahan, J. Appl. Phys. **63**, 839 (1988).

[51] L.F. Mattheiss, Phys. Rev. B **43**, 1863, 12549 (1991).

[52] M. P. C. M. Krijn and R. Eppenga, Phys. Rev. B **44**, 9042 (1991).

[53] H. Lange, M. Giehler, W. Henrion, F. Fenske, I. Sieber, and G. Oertel, Phys. Stat. Sol (b) **171**, 63 (1992).

[54] A. B. Filonov, I. E. Tralle, N. N. Dorozhkin, D. B. Migas, V. L. Shaposhnikov, G. V.

Petrov, A. M. Anishchik, and V. E. Borisenko, Phys. Stat. Sol (b) **186**, 209(1994).

[55] D. J. Poutcharovsky and E. Parthe, Acta Cryst. B **30**, 2692 (1974).

[56] C. B. Vining and C. E. Allevato, *Proc. 10th Internat. Conf Thermoelectrics*, Cardiff, Sept. 10 to 12, 8A, 1991, edited by D. M. Rowe (Babrow, Cardiff, 1991) p.167.

[57] K. Mason, G. Muller-Vogt, J. Cryst. Growth **63**, 34(1983).

[58] K. Mason and G. Muller-Vogt, J. Cryst. Growth **63**, 34 (1983).

[59] I. Engstrom, T. Lindsten, and E. Zdansky, Acta Chem. Scand. A **41**, 237 (1987).

[60] S. Peterson, J. A. Reimer, M. H. Brodsky, D. R. Campbell, F. D'Heurle, B. Karlsson, and P. A. Tove, J. Appl. Phys. **53**, 3342 (1982).

[61] H. Lange, W. Henrion, F. Fenske, T. Zettler, J. Schumann, and S. Teichert, Phys. Stat. Sol (b) **194**, 231 (1996).

[62] R. J. LaBotz, D. R. Mason, and D. F. O'Kane, J. Electrochem. Soc. **110**, 127 (1963).

[63] P. M. Lee, Phys. Rev. **135**, A1110 (1964).

[64] H. Schafer, K. H. Janzon, and A. Weiss, Agnew. Chem. Int. Ed. Engl. **2**, 393 (1963).

[65] L. M. Corliss, J. M. Hastings, W. Kunnmann, R. Thomas, and J. Zhuang, Phys. Rev. B **31**, 4337 (1985).

[66] M. A. Omar, *Elementary Solid State Physics: Principles and Applications*, (Addison-Wesley 1975).

[67] J. I. Pankove, *Optical Processes in Semiconductors*, (Dover Publications, New York, NY, 1971).

[68] A.Y. Cho, J. Crystal Growth 150 (1995) 1.

[69] M. A. Marian, H. Sitter, *Molecular Beam Epitaxy: Fundamentals and Current Studies* (Springer-Verlag, Berlin, Germany, 1989).

[70] D.M. Wood, A. Zunger: Phys. Rev B. 40, 4062 (1989)

[71] D.J. Bottomley, P. Fons, D.J. Tweet: J. Cryst. Growth 154, 401 (1995)

[72] J.Y. Tsao: *Materials fundamentals of Molecular Beam Epitaxy* (Academic, San Diego 1993)

[73] M. A. Herman, W. Richter, and H. Sitter, *Epitaxy, Physical Principles and Technical Implementations*, (Springer, Berlin, 2004).

[74] F. Bechstedt, R. Enderlein*, Semiconductor Surfaces and Interfaces—Their Atomic and Electronic Structures* (Academie, Berlin, 1988).

[75] J.M. Howe: *Interfaces in Materials* (Wiley, New York 1997)

[76] D.M. Wood, A. Zunger: Phys. Rev B. 40, 4062 (1989)

[77] D.J. Bottomley, P. Fons, D.J. Tweet: J. Cryst. Growth 154, 401 (1995)

[78] F.C. Frank, J.H. Van der Merwe: Proc. Roy. Soc., London 198, 204, 216 (1949)

[79] J.W. Matthews: Coherent Interfaces and Misfit Dislocations, in: *Epitaxial Growth Part B*, ed. By J.W. Matthews (Academic, New York 1975) p. 559.

[80] K. Ismail, B.S. Meyerson: J. Mater. Sci.: Materials in Electronics **6**, 306 (1995)

[81] E. H. Hall, American Journal of Mathematics, **2**, 287 (1879).

[82] R. L. Zrnic, *Magnetotransport Properties of $Al_xIn_{1-x}As_{1-y}Sb_y$/GaSb and Optical Properties of $GaAs_{1-x}Sb_x$*, (PhD dissertation, May 2003).

[83] L. J. Mitchell, O. W. Holland, A. Neogi, J. Li, F. D. McDaniel, J. Non-Cryst. Solids **352**,

2408 (2006).

[84] P.Y. Dusausoy, J. Protas, R. Wandji, and B. Roques, Acta Crys. B **27**, 1209 (1971).

[85] N. E. Christensen, Phys. Rev. B **42**, 7148 (1990).

[86] J. van Ek and P. E. A. Turchi, Phys. Rev. B **54** 7897(1996).

[87] M. E. Schlesinger, Chem. Rev. **90**, 607 (1990).

[88] H. M. Al-Allak and S. J. Clark, Phys. Rev B **63**, 033311 (2001).

[89] J. Tani and H. Kido, J. Solid State Chem. **169**, 19 (2002).

[90] H. Chen, P. Han, X. D. Huang, L. Q. Hu, Y. Shi, and Y. D. Zhenga, Appl. Phys. Lett. **69**, 1912 (1996).

[91] Y. Murakami, A. Kenjo, T. Sadoh, T. Yoshitake, M. Itakura, and M. Miyao, Mater. Res. Soc. Symp. Proc. **796**, V2.9.1 (2004).

[92] H. Lange, Phys. Stat. Sol. B **201**, 3 (1997).

[93] S. Eisebitt, J. E. Rubensson, M. Nicodemus, T. Boske, S. Blugel, W. Eberhardt, K. Radermacher, S. Mantl, and G. Bihlmeyer, Phys Rev. B **50**, 18330 (1994).

[94] L. Miglio, V. Meregalli, and O. Jepsen, Appl. Phys. Lett. **75**, 385 (1999).

[95] J. van Ek, P. E. A. Turchi, and P. A. Sterne, Phys. Rev. B **54**, 7897 1996).

[96] N. E. Christensen, Phys. Rev. B **42**, 7148 (1990).

[97] R. Eppenga, J. Appl. Phys. **68**, 3027 (1990).

[98] L. Miglio and V. Meregalli, J. Vac. Sci. Tech. B **16**, 1604 (1998).

[99] S. J. Clark, H. M. Al-Allak, S. Brand, and R. A. Abram, Phys. Rev. B **58**, 10389 (1998).

[100] A. G. Birdwell, *Optical Properties of Semiconducting Transition Metal Silicides*, (PhD

dissertation, 2001).

[101] A. B. Filonov, D. B. Migas, V. L. Shaposhnikov, N. N. Dorozhkin, G. V. Petrov, V. E. Borisenko, W. Henrion, and H. Lange, J. Appl. Phys. **79**, 7708 (1996)

[102] M. De Crescenzi, G. Gaggiotti, N. Motta, F. Patella, A. Balzarotti, G. Mattogno, and J. Derrien, Surface Science **251/252**, 175 (1991).

[103] R. Wandji, Y. Dusausoy, J. Protas, and B. Roques, C. R. Acad. Sci. Paris **267**, 1587 (1968).

[104] Ch. Kloc, E. Arushanov, M. Wendl, H. Hohl, U. Malang, and E. Bucher, J. Alloys Comp. **219**, 93 (1995).

[105] L. J. Chen, S. Y. Chen, and H. C. Chen, Thin Solid Films **515**, 8140 (2007).

[106] H. C. Chen, K. F. Liao, S. W. Lee, S. L. Cheng, and L. J. Chen **461** 44 (2004).

[107] Y. Nakamura, Y. Nagadomi, S.-P. Cho, N. Tanaka, and M. Ichikawa, J. Appl. Phys. **100**, 044313 (2006).

[108] H. Qi, C. Qian, and J. Liu, Nano Lett. **7**, 2417 (2007).

[109] Y. L. Chueh, L. J. Chou, S. L. Cheng, L. J. Chen, C. J. Tsai, C. M. Hsu, S. C. Kung, Appl. Phys. Lett. **87**, 223113 (2005).

[110] A. L. Schmitt, M. J. Bierman, D. Schmeisser, F. J. Himpsel, and S. Jin, Nano Lett. **6**, 1617 (2006).

[111] D. N. Leong, M. Harry, K. J. Reeson, and K. P. Homewood, Nature **387**, 686 (1997).

[112] T. D. Hunt, K. J. Reeson, K. P. Homewood, S. W. Teon, R. M. Gwilliam, and B. J. Sealy, Nucl. Instrum. Methods B **84**, 168 (1994).

[113] K. Radermacher, R. Carius, and S. Mantl, Nucl. Instrum. Methods B **84**, 163 (1994).

[114] N. A. Drozdov, A. A. Patrin, and V. D. Tkachev, Sov. Phys. JETP Lett. **23**, 597 (1976).

[115] M. G. Grimaldi, S. Coffa, C. Spinella, F. Marabelli, M. Galli, L. Miglio, and V. Meregalli, J. Lumin. **80**, 467 (1999).

[116] C. Spinella, S. Coffa, C. Bongiorno, S. Pannitteri, and M. G. Grimaldi, Appl. Phys. Lett. **76**, 173 (2000).

[117] C. Spinella, S. Coffa, C. Bongiorno, S. Pannitteri, and M. G. Grimaldi, Appl. Phys. Lett. **76**, 173 (2000).

[118] B. Schuller, R. Carius, S. Lenk, and S. Mantl, Micro. Eng. **60**, 205 (2002).

[119] M. Takauji, N. Seki, T. Suemasu, F. Hasegawa, and M. Ichida, J. Appl. Phys. **96**, 2561 (2004).

[120] A. G. Birdwell, T. J. Shaffner, D. Chandler-Horowitz, G. H. Buh, M. Rebien, W. Henrion, P. Stauß, G. Behr, L. Malikova, F. H. Pollak, C. L. Littler, R. Glosser, and S. Collins, J. Appl. Phys. **95**, 2441 (2004).

[121] A. G. Birdwell, C. L. Littler, R. Glosser, M. Rebien, W. Henrion, P. Stauß, and G. Behr, Appl. Phys. Lett. **92**, 211901 (2008).

[122] J. E. Mahan, V. L. Thanh, J. Chevrier, I. Berbezier, J. Derrien, and R. G. Long, J. Appl. Phys. **74**, 1747 (1993).

[123] K. Hossain, *A Novel Process for GeSi Thin Film Synthesis*, (PhD dissertation, 2007).

[124] M. Rebien, W. Henrion, U. Muller, and S. Gramlich, Appl. Phys. Lett. **74**, 970

(1999).

[125] W. L. Korst, L. N. Finnie, and A. W. Searcy, J. Phys. Chem. B **67** 1541 (1957).

[126] I. Engstrom, Acta Chem. Scand, **24** 2117 (1970).

[127] K. Mason and G. Muller-Vogt, J. Cryst. Growth **63** 34 (1983).

[128] D. J. Poutcharovsky and E. Parthe, Acta Cryst. B **30** 2692 (1974).

[129] C. S Petersson, J. E. E. Baglin, J. J. Dempsey, F. M. D'Heurle, and S. J. La Placa, J. Appl. Phys. **53** 4866 (1982).

[130] L. Schellenberg, H. F. Braun, and J. Muller, J. Less-Common Met. **144** 341 (1988).

[131] Y. S. Chang and M. L. Chou, J. Appl. Phys. **66** 3011 (1989).

[132] D. B. Migas, W. Henrion, M. Rebien, V. L. Shaposhnikov, V. E. Borisenko, and L. Miglio, Opt. Materials, **17** 335 (2001).

[133] A. Ishizaka and Y. Shiraki, J. Electrochem. Soc. **133**(4), 666 (1986).

[134] C.S. Petersson, J.E.E. Baglin, J.J. Dempsey, F.M. d'Heurle, S.J. La Placa, J. Appl. Phys. **53**, 4866 (1982).